What is the Right Level of Activation of a High-Spin {FeNO}[7] Complex to Enable Direct N-N Coupling? Mechanistic Insight into Flavodiiron NO Reductases

Hai T. Dong[a], **Stephanie Camarena**[a], **Debangsu Sil**[b], **Michael O. Lengel**[a], **Jiyong Zhao**[c], **Michael Y. Hu**[c], **E. Ercan Alp**[c], **Carsten Krebs**[b,d], **Nicolai Lehnert**[a]

[a]Department of Chemistry and Department of Biophysics, The University of Michigan, Ann Arbor, Michigan 48109-1055, United States

[b]Department of Chemistry, The Pennsylvania State University, University Park, Pennsylvania 16802, United States

[c]Advanced Photon Source (APS), Argonne National Laboratory (ANL), Argonne, Illinois 60439, United States

[d]Department of Biochemistry and Molecular Biology, The Pennsylvania State University, University Park, Pennsylvania 16802, United States

Abstract

Flavodiiron nitric oxide reductases (FNORs), found in pathogenic bacteria, are capable of reducing nitric oxide (NO) to nitrous oxide (N_2O) to detoxify NO released by the human immune system. Previously, we reported the first FNOR model system that mediates direct NO reduction (Dong et al., *J. Am. Chem. Soc.* **2018**, *140*, 13429–13440), but no intermediate of the reaction could be observed. Here we present a new set of model complexes that, depending on the ligand substitution, can either mediate direct NO reduction or stabilize a highly activated high-spin (hs) {FeNO}[7] complex, the first intermediate of the reaction. The precursors, [{Fe^{II}(MPA-(RPhO)$_2$)}$_2$] (**1**, R = H and **2**, R = ^{t}Bu, Me), were prepared first and fully characterized. Complex **1** (without steric protection) directly reduces NO to N_2O almost quantitatively, which constitutes only the second example for this reaction in model systems. Contrarily, reaction of sterically protected **2** with NO forms the stable mononitrosyl complex **3**, which shows one of the lowest N-O stretching frequencies (1689 cm^{-1}) observed so far for a mononuclear hs-{FeNO}[7] complex. This study confirms that an N-O stretch ~1700 cm^{-1} represents the appropriate level of activation of the FeNO unit to enable direct NO reduction. The higher activation level of these hs-{FeNO}[7] complexes compared to those formed in FNORs emphasizes the importance of hydrogen bonding

---

Corresponding Author: lehnertn@umich.edu.

ASSOCIATED CONTENT:

Supporting Information:

The Supporting Information is available free of charge at _____ and contains information on the following: Crystallographic parameters, optimized DFT coordinates, N_2O yield quantifications, NRVS, EPR, IR, UV-Vis, and Mössbauer spectroscopic data for complexes **1**-**3**. Supplementary crystallographic data can be found at the CCDC with deposition numbers #2078941, #2078934, and #2081128 and can be obtained free of charge.

Notes:

The authors declare no competing financial interest

residues in the active sites of FNORs to activate the bound NO ligands for direct N–N coupling and N$_2$O formation. The implications of these results for FNORs are further discussed.

Graphical abstract

I. Introduction

Nitric oxide (NO) is an important molecule in mammalian physiology and it performs different functions depending on its concentration.[1] For example, at low, nanomolar concentration NO functions in neuronal signal transduction, regulation of blood pressure, the control of blood clotting, and other important physiological functions in humans.[2–4] At micromolar concentrations, on the other hand, NO is acutely toxic and is utilized by mammals for immune defense.[5] For example, macrophages use NO besides other toxic chemicals to kill invading pathogens.[6] However, over time, a number of pathogens (e.g. *Escherichia coli*, *Desulfovibrio gigas*, *Moorella thermoacetica*, *Trichomonas vaginalis*, *Klebsiella pneumoniae*, *Salmonella typhimurium*, etc.) have evolved a sophisticated defense system against NO and nitrosative stress.[7–13] Here, transcription factors are used to sense NO,[7] and upon detection of NO, expression of flavodiiron nitric oxide reductases (FNORs) is induced as a defense mechanism against NO toxicity and attack by our immune system.[7–9] These enzymes reduce NO to less toxic N$_2$O, allowing the pathogens to proliferate in the human body, causing chronic infections that are difficult to cure.[14–18] Because of their significance in bacterial pathogenesis in humans, FNORs are important research targets for the development of new therapeutics, especially against drug resistant strains.[19–22] One important piece of this puzzle is the elucidation of the mechanism of FNORs. Specifically, this includes the determination of the role that the diiron core and the flavin cofactor in the active sites of these enzymes play for catalysis, which is the key to our understanding of the mechanism of these enzymes. Besides the work on FNORs themselves, model complexes have played a critical role in elucidating different mechanistic possibilities for these enzymes.[1,23,24]

FNORs are members of the large family of flavodiiron proteins (FDPs), which are commonly found in microaerobes and serve as O$_2$ scavengers, catalyzing the non-metabolic reduction of O$_2$ to water.[25] Stopped-flow UV-Vis and rapid freeze quench Mössbauer studies by Kurtz and coworkers on the *Thermotoga maritima* FDP (*Tm* FDP) have shown that these enzymes are catalytically active when their non-heme diiron active sites are in the diferrous state.[26] In the first step of the reaction, two molecules of NO bind to the diiron core to form a dinitrosyl complex, a [hs-{FeNO}^{7}]$_2$ species in the Enemark-

Feltham notation (where the superscripted number (7) is the sum of the number of Fe(d) and NO(π*) electrons),[27] as the catalytically competent intermediate.[28–30] Single turnover experiments on the *T. maritima* FDP have provided strong evidence that the resulting [hs-{FeNO}^{7}]$_2$ intermediate itself can support N-N coupling and N$_2$O formation (the "*direct NO reduction*" mechanism; see Scheme 1, top).[29] This is in contrast to many model systems, where the [hs-{FeNO}^{7}]$_2$ complex is stable and needs reductive activation to proceed to N$_2$O formation (commonly by one-electron reduction, via the so-called "*semireduced*" mechanism; see Scheme 1, bottom).[31–33]

In agreement with the experimental results, recent mechanistic studies by Van Stappen et al. using density functional theory (DFT) calculations on our model system [Fe$_2$(BPMP) (OPr)(NO)$_2$]$^{2+}$ have shown that this stable [hs-{FeNO}^{7}]$_2$ complex can be activated by one-electron reduction, leading to N-N coupling to form a cis-hyponitrite intermediate.[34] The calculated activation barrier for N-N bond formation in this complex is 13.7 kcal/mol. Recent experimental results further indicate that it is essential to have the right conformation, with the two [FeNO] units in a coplanar (or syn/cis) arrangement, for N-N coupling to occur,[35] and that even relatively small distortions of the [FeNO]$_2$ core profoundly affect N$_2$O yields.[36] In [Fe$_2$(BPMP)(OPr)(NO)$_2$]$^{2+}$, one-electron reduction of one of the hs-{FeNO}^{7} centers to the hs-{FeNO}^{8} state provides the necessary activation to allow for the N-N coupling reaction to proceed. The DFT calculations predict that the increased activation of the reduced hs-{FeNO}^{8} unit is reflected by a shift of the N-O stretch below 1700 cm^{-1}. However, this prediction could not be confirmed experimentally due to the very short lifetime of the proposed intermediate.[33] We speculated that a sufficiently activated [hs-{FeNO}^{7}]$_2$ complex might be able to mediate direct NO reduction, without the need for additional reducing equivalents. This level of activation would be indicated by a low N-O stretching frequency of 1700 cm^{-1}. Such low N-O stretching frequencies are quite unusual for hs-{FeNO}^{7} complexes, and in fact, there is only one report for such a compound from the Goldberg group.[37] This hypothesis is further supported by the high degree of stability of all of the reported [hs-{FeNO}^{7}]$_2$ model complexes in the literature, which all show ν(N-O) > 1750 cm^{-1}.[31–33,35,38,39] However, this hypothesis still awaits experimental verification.

In a follow-up study, we were able to show that the electron-rich complex [CoCp$_2$][Fe$^{II}_2$((Py$_2$PhO$_2$)MP)(OAc)$_2$] ((Py$_2$PhO$_2$)MP^{3-} = 2,6-Bis[((2-hydroxybenzyl)(2-pyridylmethyl)amino)methyl]-4-methylphenol trianion) can in fact mediate direct NO reduction.[40] Here, (Py$_2$PhO$_2$)MP^{3-} is a derivative of the initially used ligand BPMP$^-$ where two Py (pyridine) donors (one per iron center) are replaced by strongly donating phenolate groups (Scheme 2, left). This complex is less biomimetic, as it features phenolate donors that are not present in FNOR active site, but allows us to adjust the electronic properties of the iron centers to make them more electron-rich. This diferrous complex is highly reactive with NO and can perform multiple cycles of direct NO reduction to produce N$_2$O quantitatively in the presence of excess protons and reductant.[40] The product after reaction of this complex with NO is a ferric μ-oxo complex (as shown by Mössbauer spectroscopy), confirming that the complex does indeed perform NO reduction and **not** NO disproportionation. However, due to its fast reaction rate, no NO-bound species could

be isolated under ambient reaction conditions for this model complex. Some evidence for NO-bound species was obtained in low-temperature IR studies, which indicate hs-$\{FeNO\}^7$ adducts with low N-O stretching frequencies of 1705–1730 cm^{-1}.[40] Computational results further support the idea that hs-$\{FeNO\}^7$ complexes with N-O stretching frequencies 1700 cm^{-1} are activated for direct N-N coupling.[40] Going forward, this presented us with the unique challenge to construct a model system with a similar level of activation as the NO-bound intermediate of $[Fe^{II}_2((Py_2PhO_2)MP)(OAc)_2]^-$, but where NO reduction was somehow stalled, allowing us to isolate and study the electronic properties of the corresponding hs-$\{FeNO\}^7$ complex that has the right level of activation for direct NO reduction. In contrast, the N-O stretching frequency of the critical diiron dinitrosyl intermediate in FNORs is located at about 1750 cm^{-1},[1] clearly indicating that FNORs are able to catalyze direct NO reduction with distinctively less activated [FeNO] units. This interesting dichotomy is further analyzed in the Discussion section.

In order to tackle this problem, we decided to take advantage of the fact that efficient NO reduction to N_2O seems to require a diiron complex.[23,31–33,38,39] We therefore designed a new ligand system that corresponds to half of the $H_3[(Py_2PhO_2)MP]$ ligand (Scheme 2, right) to promote the formation of corresponding, _mononuclear_ complexes. Isolation of a highly activated mononuclear hs-$\{FeNO\}^7$ complex would in turn further support the hypothesis that diiron complexes are critical to allow for efficient NO reduction to occur. The ligand $H_2[MPA-(^tBuMePhO)_2]$ is decorated with a sterically protecting _tert_-butyl (^tBu) substituent to potentially stabilize a reactive nitrosylated species. The use of steric shielding is a strategy that is often employed in synthetic inorganic chemistry.[41–49] Iron complexes of the resulting ligand system, $H_2[MPA-(^tBuMePhO)_2]$, were then studied in direct comparison to those of the unfunctionalized version of this ligand, $H_2[MPA-(PhO)_2]$. Excitingly, whereas the bulky ligand allowed for the isolation and characterization of a highly activated hs-$\{FeNO\}^7$ complex, the ferrous complex of the unfunctionalized ligand undergoes N-N coupling and N_2O formation, following the direct NO reduction mechanism. This is only the second demonstration of this reaction in a model complex. The highly activated, mononuclear hs-$\{FeNO\}^7$ complex was further studied using a number of spectroscopic methods, including UV-Vis, IR, Mössbauer and Nuclear Resonance Vibrational Spectroscopy (NRVS). This complex corresponds to an unusual, non-classical hs-$\{FeNO\}^7$ species with partial coligand oxidation. These results are summarized in this paper.

II. Experimental Section

Reactions were generally performed using inert gas (Schlenk) techniques. All solvents were dried and freeze pump thawed to remove dioxygen and water. Preparation and handling of air-sensitive materials was performed under a dinitrogen atmosphere in an MBraun glovebox, equipped with a circulating purifier (O_2, H_2O <0.1 ppm). Nitric oxide (99.95%) was first passed through an Ascarite II column and then a −80 °C cold trap to remove higher nitrogen oxide impurities prior to use.

Bis(2-hydroxybenzyl)(2-pyridylmethyl)amine ($H_2[MPA-(PhO)_2]$) was synthesized according to published procedures.[50] **2-pyridylamino-N,N-bis(2-methylene-4-methyl-6-**

tert-butylphenol) (H$_2$[**MPA-(^tBuMePh**O)$_2$]) was prepared according to published procedures.[51] The purity of these ligands was established by ^{1}H-NMR spectroscopy (400 MHz, Chloroform-*d*; see Figures S37 and S38).

[{Fe(MPA-(PhO)$_2$)}$_2$] (1):

Under an inert atmosphere, the ligand H$_2$[MPA-(PhO)$_2$] (100 mg, 0.31 mmol) and KOMe (43.8 mg, 0.62 mmol) are dissolved in a minimal amount of MeOH (about 5 ml) and stirred for 30 minutes. 136 mg (0.31 mmol) of Fe(OTf)$_2$•2CH$_3$CN is then added into the reaction and the solution immediately turns orange. The reaction is stirred for overnight at room temperature, and MeOH is then removed under reduce pressure. The crude product mixture is re-dissolved in CH$_2$Cl$_2$, and a solid impurity is removed via filtration. The CH$_2$Cl$_2$ is then removed under reduce pressure. The crude product is dissolved in CH$_3$CN, and diethyl ether is added for precipitation. The solution is allowed to recrystallize at −33 °C overnight. The solution is then filtered under an inert atmosphere to yield a light orange product, complex **1**. Yield: 109 mg (92%). UV-Vis: λmax = 460 nm. Mössbauer: δ = 1.15 mm/s and △EQ = 2.89 mm/s.

[{Fe(MPA-(^tBuMePhO)$_2$)}$_2$] (2):

Under an inert atmosphere, in a 20 ml vial, the ligand H$_2$[MPA-(^tBuMePhO)$_2$] (200 mg, 0.435 mmol) and KOMe (61 mg, 0.87 mmol) are dissolved in a minimal amount of MeOH (about 5 ml) and stirred for 30 minutes. 190 mg (0.435 mmol) of Fe(OTf)$_2$•2CH$_3$CN is then added into the reaction and the solution immediately turns green. The reaction is stirred overnight at room temperature, and MeOH is then removed under reduce pressure. The crude product mixture is re-dissolved in CH$_2$Cl$_2$, and a solid impurity is removed via filtration. The filtrate is then layered with hexane, and recrystallization is carried out at −33 °C overnight. Filtration yields a bright green crystalline product that is suitable for X-ray crystallography. Yield: 101 mg (45%) of very pure, crystalline product. Elemental anal. calcd. for C$_{60}$H$_{76}$Fe$_2$N$_4$O$_4$ single crystals co-packed with CH$_2$Cl$_2$ (6:8 ratio): C, 63.03; H, 6.65; N, 4.90; found (%):C, 63.32; H, 6.90; N, 4.75. UV-Vis: λmax = 522 nm with a shoulder at 683 nm. Mössbauer: δ = 1.07 and △EQ = 1.68 mm/s.

[Fe(MPA-(^tBuMePhO)$_2$)(NO)] (3):

Under an inert atmosphere, in a 3-neck round bottom flask charged with a stir bar, 100 mg (0.097 mmol) of complex **2** is dissolved in a minimal amount of CH$_2$Cl$_2$ until the solution is homogeneous. Excess amount of dried and purified NO gas is then added into the gas headspace, and the solution immediately turns very dark brown. The reaction is stirred for 1 hour. The NO gas is then purged from the head space of the flask before hexane is added into the reaction mixture (from the top, with the septum removed to prevent build-up of pressure), and the solution is allowed to recrystallize at −33 °C overnight. The solution is then filtered under an inert atmosphere to yield very dark brown crystals of complex **3** that are suitable for X-ray crystallography. Yield: 30% of pure, crystalline product. Elemental anal. calcd. for C$_{30}$H$_{38}$FeN$_3$O$_3$: C, 66.18; H, 7.03; N, 7.72; found (%):C, 66.36; H, 7.27; N, 7.43. IR: ν(N–O) = 1689 cm^{-1}. UV-Vis: λmax = 455 nm. Mössbauer: δ = 0.56 mm/s and △EQ = 0.92 mm/s.

Infrared spectra of solid samples were obtained using PerkinElmer BX and GX and Bruker Alpha-E FTIR spectrometers. The IR spectra of solution samples were obtained in thin-layer solution cells equipped with CaF_2 windows. Gas IR spectra were obtained using a Pike Technologies short-path HT gas cell with 100 mm path length, equipped with CaF_2 windows, on the same instruments.

Nuclear Resonance Vibrational Spectroscopy (NRVS) measurements were performed at beam line 3-ID at the Advanced Photon Source (APS) at Argonne National Laboratory, as previously described.[52] Samples were loaded in copper sample holders with lucite lids. The samples were maintained at cryogenic temperatures using a liquid helium-cooled cryostat. Spectra of solid samples were recorded from −50 to 100 meV in 0.25 meV steps. Multiple scans were taken, normalized to the intensity of the incident beam, and added together to achieve good signal to noise; the final spectrum represents averages of 7 scans. The program Phoenix4 was used to convert the raw NRVS data to the vibrational density of states (VDOS).[53,54]

UV-Vis/Immersion Probe. UV-Vis spectra were obtained using an Analytic Jena Specord S600 UV-Vis spectrometer. Dip probe experiments used the same spectrometer, with a Hellma low-temperature immersion probe.

^{1}H-NMR spectra were recorded on a Varian Inova 400 MHz instrument and referenced against residual solvent signals.

Electron paramagnetic resonance spectra were obtained on a Bruker-X-band EMX spectrometer equipped with Oxford Instruments liquid nitrogen and liquid helium flow cryostats. EPR spectra were typically obtained on frozen solutions using ~20 mW microwave power and 100 kHz field modulation with the amplitude set to 1 G. Sample concentrations were ~2 mM, and ~ 4 mM for reaction products.

Elemental analysis:

Elemental analyses were conducted by Atlantic Microlabs (Norcross, GA).

Cyclic Voltammetry:

Cyclic voltammograms (CVs) were obtained on a CH Instruments CHI600E electrochemical workstation with a glassy-carbon working electrode, a platinum counter electrode, and a silver wire pseudoreference electrode. After each experiment, ferrocene (Fc) was added to the solution and a cyclic voltammogram was taken under the same experimental conditions as a reference. All potentials were referenced to the Fc^+/Fc standard. Data were collected on ~5 mM samples in CH_2Cl_2 with 0.1M tetrabutylammonium hexafluorophosphate ([TBA][PF_6]) as the supporting electrolyte.

Structure Determination:

Green prisms of **[{Fe(MPA-([t]BuMePhO)$_2$)}$_2$]** were grown from a dichloromethane/hexanes solution of the compound at −33 °C, and a crystal of dimensions 0 .10 x 0 .10 x 0 .06 mm was used for structural analysis. Brown blocks of **[Fe(MPA-([t]BuMePhO)$_2$)(NO)]** were grown from a dichloromethane/hexanes solution of the compound at −33 °C, and a

crystal of dimensions 0 .22 x 0 .16 x 0 .14 mm was used for structural analysis. Pale yellow needles of **[Fe{Fe(MPA-(Ph**O)$_2$**)}(HCO**O)$_2$**]$_8$** were grown by diffusion of diethyl ether into an acetonitrile solution of [{Fe(MPA-(Ph$O)_2$)}$_2$] at 20 °C. A crystal of dimensions 0 .05 x 0 .02 x 0 .02 mm was used for structural analysis. The crystals were mounted on a Rigaku AFC10K Saturn 944+ CCD-based X-ray diffractometer equipped with a low temperature device and a Micromax-007HF Cu-target micro-focus rotating anode (λ = 1.54187 Å) operated at 1.2 kW power (40 kV, 30 mA). The X-ray intensities were measured at 85(1) K with the detector placed at a distance of 42.00 mm from the crystal. A total of 2028 images were collected with an oscillation width of 1.0° in ω. Rigaku d*trek images were exported to CrysAlisPro for processing and corrected for absorption.

For **[{Fe(MPA-(^{t}BuMePh**O)$_2$**)}$_2$]**, the exposure times were 1 sec. for the low angle images, 5 sec. for high angle. The integration of the data yielded a total of 43,386 reflections to a maximum 2θ value of 138.64° of which 5421 were independent and 5012 were greater than $2\sigma(I)$. The final cell constants (Table S1) were based on the xyz centroids of 17,458 reflections above $10\sigma(I)$. Analysis of the data showed negligible decay during data collection. The structure was solved and refined with the Bruker SHELXTL (version 2018/3) software package, using the space group C2/c with Z = 4 for the formula $C_{62}H_{80}N_4O_4Cl_4Fe_2$. All non-hydrogen atoms were refined anisotropically with the hydrogen atoms placed in idealized positions. The complex lies on a two-fold rotation axis. Full matrix least-squares refinement based on F^2 converged at R1 = 0.0431 and wR2 = 0.1176 [based on I>2sigma(I)], R1 = 0.0467 and wR2 = 0.1214 for all data. Additional details are presented in Table S1 and are given as Supporting Information in a CIF file.

For **[Fe(MPA-(^{t}BuMePh**O)$_2$**)(NO)]** the exposure times were 1 sec. for the low angle images, 3 sec. for high angle. The integration of the data yielded a total of 19,767 reflections to a maximum 2θ value of 138.57° of which 4905 were independent and 4847 were greater than $2\sigma(I)$. The final cell constants (Table S7) were based on the xyz centroids of 17,758 reflections above $10\sigma(I)$. Analysis of the data showed negligible decay during data collection. The structure was solved and refined with the Bruker SHELXTL (version 2018/3) software package, using the space group P1bar with Z = 4 for the formula $C_{30}H_{38}N_3O_3Fe$. All non-hydrogen atoms were refined anisotropically with the hydrogen atoms placed in idealized positions. Full matrix least-squares refinement based on F_2 converged at R1 = 0.0408 and wR2 = 0.1139 [based on I>2sigma(I)], R1 = 0.0412 and wR2 = 0.1143 for all data. Additional details are presented in Table S7 and are given as Supporting Information in a CIF file.

For **[Fe{Fe(MPA-(Ph**O)$_2$**)}(HCO**O)$_2$**]$_8$**, the exposure times were 10 sec. for the low angle images, 80 sec. for high angle. The integration of the data yielded a total of 79,913 reflections to a maximum 2θ value of 141.07° of which 19,891 were independent and 10,946 were greater than $2\sigma(I)$. The final cell constants (Table S13) were based on the xyz centroids of 12,043 reflections above $10\sigma(I)$. Analysis of the data showed negligible decay during data collection. The structure was solved and refined with the Bruker SHELXTL (version 2018/3) software package, using the space group I-4 with Z = 4 for the formula $C_{176}H_{160}N_{16}O_{48}Fe_{16}$. All non-hydrogen atoms were refined anisotropically with

the hydrogen atoms placed in idealized positions. The structure has two independent Fe_{16} clusters each on a −4 symmetry site of the lattice. Full matrix least-squares refinement based on F^2 converged at R1 = 0.0804 and wR2 = 0.2107 [based on I>2sigma(I)], R1 = 0.1351 and wR2 = 0.2700 for all data. The SQUEEZE subroutine of the PLATON program suite was used to address the disordered solvent contained in solvent accessible voids present in the structure. Additional details are presented in Table S13 and are given as Supporting Information in a CIF file.

Mössbauer spectroscopy.—The Mössbauer sample of **1** was prepared by metalating the ligand, $H_2[MPA-(PhO)_2]$, with $^{57}Fe(OTf)_2$ using the same procedure mentioned above. The subsequent preparation of samples of the reaction product of complex **1** with NO gas was carried out in DMF at 6 mM concentration. Solution samples were withdrawn from the sealed round-bottom flask and immediately frozen in Mössbauer cups in a cold well under inert atmosphere. Complexes **2** and **3** were prepared using the procedures mentioned above. The sample of complex **2** was prepared by grinding the appropriate amount of material with boron nitride. The sample of complex **3** was prepared by dissolving the complex into DMF at 5 mM concentration. Mössbauer spectra were recorded on an alternating constant acceleration Mössbauer spectrometer from SEE Co. (Edina, MN) equipped with a Janis SVT-400 variable-temperature cryostat. The external 53 mT magnetic field was oriented parallel or perpendicular, as needed, to the direction of propagation of the γ beam. All isomer shifts are quoted relative to the centroid of the spectrum of α-iron metal at room temperature. Simulation of the Mössbauer spectra was carried out using the WMOSS spectral analysis software (www.wmoss.org; Seeco Research, Edina, MN).

DFT calculations.—Gaussian 09 was used to carry out all of the geometry optimizations and frequency calculations performed here.[55] The optimization of the broken symmetry structures of the putative dinitrosyl intermediates was performed with the gradient-corrected functional BP86, which has been shown to give good geometric structures for related hs-$\{MNO\}^n$ species,[34] and the TZVP basis set. Frequency calculations of the resulting, optimized structures were further performed in all cases to ensure that proper energy minima had been obtained, and to determine the predicted N-O stretching frequencies. Additionally, calculations with the hybrid functional B3LYP and the TZVP basis set were performed for the species of interest. The program ORCA was used to perform single point calculations and to calculate Mössbauer parameters.[56]

IR Gas Headspace Analysis for N_2O Detection.—N_2O quantification was carried out by gas headspace analysis using infrared spectroscopy. The general protocol for gas headspace analysis is described in ref. [57]. Here, ~6.73 mg of complex **1** in 2.5 mL of DMF were reacted with ~4–6 ml of NO gas in a sealed 25 ml round-bottom flask, before the headspace was transferred by vacuum to a sealed gas IR cell with CaF_2 windows. Quantification of N_2O was performed via integration of the prominent IR features at 2235 and 2212 cm^{-1} of this molecule (N-N stretching vibration) against separately determined

N$_2$O standards (using Piloty's acid). Using this calibration method, a maximum N$_2$O yield of 81% ±5% was obtained for **1**. The error caused by the somewhat different solubility of N$_2$O in water (used to generate the calibration curve with Piloty's acid) and organic media (at the concentrations used for the experiments) is well within ±5%.

III.   Results and Analysis

As described in the Introduction, we prepared two derivatives of the H$_2$[MPA-(RPhO)$_2$] ligand (with R = H and R = ^{t}Bu, Me) to model half of the H$_3$[(Py$_2$PhO$_2$)MP] ligand (see Scheme 2), which we used successfully in the complex [Fe^{II}$_2$((Py$_2$PhO$_2$)MP)(OAc)$_2$]$^-$ to model the direct NO reduction pathway of FNORs. The ligand H$_2$[MPA-(^{t}BuMePhO)$_2$] features bulky ^{t}Bu groups on the phenolates to stabilize mononuclear complexes. Both H$_2$[MPA-(PhO)$_2$] and H$_2$[MPA-(^{t}BuMePhO)$_2$] were prepared using published procedures.[50,51] The obtained ligands were characterized by ^{1}H-NMR spectroscopy (see Figures S35 and S36). Metalation then yields the corresponding ferrous complexes **1** and **2** with these ligands, which are extremely air sensitive (especially complex **1**). Therefore, fresh batches of the ferrous complexes have to be prepared prior to conducting any experiments.

III.1.   Synthesis and Characterization of the Ferrous Complexes with Ligands H$_2$[MPA-(PhO)$_2$] and H$_2$[MPA-(^{t}BuMePhO)$_2$]

The ligand H$_2$[MPA-(^{t}BuMePhO)$_2$] (2-pyridylamino-N,N-bis(2-methylene-4-methyl-6-tert-butylphenol)) is metalated by first deprotonating the phenol groups using KOMe in MeOH, followed by addition of one equivalent of Fe(OTf)$_2$. MeOH is then removed under reduced pressure, and the crude product is re-dissolved in CH$_2$Cl$_2$, filtered, and recrystallized to obtain the pure, bright green crystalline product **2**. Complex **2** is characterized by a very broad absorption band at 522 nm with a small shoulder at 683 nm (see Figure 1). As mentioned above, we had designed the ligand H$_2$[MPA-(^{t}BuMePhO)$_2$] to give a mononuclear complex. However, to our surprise, X-ray crystallography of a single-crystalline green prism of **2**, grown from slow diffusion of hexane into a saturated CH$_2$Cl$_2$ solution of **2** at −33 °C, revealed that **2** has a dimeric structure, [{Fe^{II}(MPA-(^{t}BuMePhO)$_2$)}$_2$]. As shown in Figure 2, in the crystal structure two monomers are bridged through the phenolate arms of the ligand, even in the presence of the bulky *tert*-butyl substituents in the second coordination sphere (SCS). The Fe-Fe distance in **2** is unusually short, 2.98 Å. Each iron center is penta-coordinated with an adjacent, open coordination site with a τ5 parameter of 0.16, indicating a pseudo square pyramidal geometry. The structure of **2** further reveals that the two open coordination sites are in trans position to each other. The Fe$_2$O$_2$ diamond core is slightly asymmetric, with Fe-O(Ph) bond distances of 2.12 and 2.04 Å, respectively. Complex **2** is EPR silent due to both iron centers being high-spin (hs) Fe(II). The 4.2-K/53-mT Mössbauer spectrum reveals a quadrupole doublet with an isomer shift (δ) of 1.07 mm/s and a quadrupole splitting (△EQ) of 1.68 mm/s (Figure S31). The isomer shift is typical of hs-Fe(II).[58] While the quadrupole splitting parameter is smaller than those of typical hs-Fe(II) complexes, such a small value has been seen before[59] and could be caused by quantum-mechanical admixture of low-lying exciting electronic states. This conclusion is further supported by studies on similar complexes reported in

the literature, which indicate that H_2[MPA-(RPhO)$_2$]-type coligands generally stabilize the high-spin state of iron.[60,61]

The ferrous complex **1** was synthesized by metalation of H_2[MPA-(PhO)$_2$] with Fe(OTf)$_2$, using a similar protocol as described above for complex **2**, and obtained as a light orange product. Unlike complex **2**, complex **1** is unstable and is oxidized even at very low concentrations of O_2 and other, minor contaminants in the glovebox atmosphere. Based on the structure of **2** shown in Figure 2, we assumed that **1** also has a dimeric structure in solution, [{Fe(MPA-(PhO)$_2$)}$_2$], but further oligomerization is possible, as observed for similar types of ligands in previous studies.[62–65] Efforts to characterize complex **1** with X-ray diffraction proved to be difficult due to its high sensitivity towards residual O_2, and its predisposition to form very fine needles that do not sufficiently diffract for structural analysis. We were ultimately able to obtain a crystal structure of a partially decomposed form of the complex, which shows that the complex can form larger oligomeric structures, using again the phenolate groups as bridges (see Figure S7 and accompanying text). A recent publication further confirms that complexes with H_2[MPA-(PhO)$_2$]-type ligands can indeed form multinuclear complexes with more than two metal centers.[66] Characterization of freshly prepared samples of complex **1** by Mössbauer spectroscopy, either in solution or in solid, revealed the presence of a single quadrupole doublet with an isomer shift (δ) of 1.15 mm/s and a quadrupole splitting ($\triangle$EQ) of 2.89 mm/s (see Figure S1 and S30), which are typical of hs-Fe(II) centers.[58] The observation of a single quadrupole doublet suggests that freshly prepared **1** does not contain the oligomeric structure with two distinct Fe(II) sites that was crystallized out over time. Instead, freshly prepared **1** has likely a dimeric structure, [{Fe^{II}(MPA-(PhO)$_2$)}$_2$], similar to that of **2** (see Figure 2). The absorption spectrum of **1** in CH_2Cl_2 exhibits a weak band at 460 nm, as shown in Figure 1. Complex **1** is EPR silent due to the presence of hs-Fe(II) centers.

The cyclic voltammogram (CV) of complex **2** shows two oxidative events at −0.32 and 0.26 V vs Fc$^+$/Fc (see Figure S36), corresponding to the Fe(II)Fe(II)/Fe(II)Fe(III) and Fe(II)Fe(III)/Fe(III)Fe(III) couples of the dimer. The complex is stable under the CV experimental conditions, and only shows a small signal of a corresponding monomer, at −0.01 V. In comparison, complex **1** is less stable under these conditions, and besides the two oxidative waves for the dimer at −0.42 and 0.17 V vs Fc$^+$/Fc, exhibits a distinctive monomer signal at −0.14 V (see Figure S35). However, the oxidized forms of complexes **1** and **2** are clearly unstable, showing a multitude of reductive signals on the return scan, as shown in Figures S35 and S36. These results further indicate small electronic differences between **1** and **2**, with **1** having more negative oxidative potentials by about 10 mV.

III.2. Reactivity of Complex 2 with NO Gas: A Highly-Activated hs-{FeNO}^{7} Complex

Exposure of the dimeric complex **2** to NO gas led to an immediate color change of the solution from green to dark brown. The solution was then charged with hexane, and a clean, dark brown single-crystalline product was obtained after further recrystallization at −33 °C. X-ray diffraction data of the brown block-shaped crystals revealed the formation of the unique, pseudo trigonal-bipyramidal mononitrosyl complex, [Fe(MPA-(^{t}BuMe-PhO)$_2$)(NO)] (**3**), as shown in Figure 3. Hence, although the ferrous precursor complex **2** is dimeric,

the steric bulk provided by the ^{t}BuMe-PhO$^-$ arms forces the NO complex to become monomeric, which stabilizes the complex against further reactions (see Section III.3). Complex **3** is very sensitive and readily loses NO under vacuum; however, this complex is stable in the solid state at room temperature under an inert atmosphere. Interestingly, **3** shows Fe-NO and N-O bond distances of 1.79 Å and 1.15 Å, respectively, which is in line with other hs-{FeNO}^{7} complexes previously characterized that contain phenolate ligands (see Table S20). For example, the related complex [Fe(BMPA-^{t}Bu2PhO)(OTf)(NO)] (**4**) with a monophenolate coligand shows Fe-NO and N-O bond distances of 1.78 Å and 1.10 Å, respectively (see Table S20).[67] The Fe-N-O bond angle of **3** is 149°, which is surprising, since the FeNO bonds of complexes with steric bulk in the SCS are usually closer to linear.[68] On the other hand, the small Fe-N-O angle is again in agreement with the large degree of NO reduction in **3**.[69] Interestingly, the NO moiety is bent towards the bulky tert-butyl group in the SCS, and not towards the pyridine ring, which we attribute to crystal packing effects in the solid state, and possibly the formation of an unusual CH---ON agostic interaction (CH---ON distance: 2.69 Å). The Fe-O(Ph) bond distances are 1.90 and 1.92 Å, respectively, and the Fe-N(Py) bond length is 2.14 Å. The $\tau 5$ parameter for **3** is 0.83 indicating a pseudo trigonal-bipyramidal geometry.

Complex **3** is characterized by an absorption band at 455 nm in the UV-Vis spectrum (Figure 1) and shows an EPR spectrum with major signals at $g_{eff} = 4, 2$, typical for an axial $S_t = 3/2$ complex, and consistent with a hs-{FeNO}^{7} compound (see Figure S33). The $S_t = 3/2$ ground state can be rationalized by antiferromagnetic coupling between the hs-Fe(III) center ($S = 5/2$) and the ^{3}NO$^-$ ligand ($S = 1$).[70] What is unusual about the EPR spectrum of **3** is the splitting of the $g_{eff} = 4$ signal into a large number of lines, depending on the solvent used for the EPR measurements. However, since the observed pattern is not reproducible between solvents (see Figure S34 for EPR spectra in toluene, DMF and THF), we believe that this is due to incomplete dissolution of the complex at low temperature, leading to residual intermolecular couplings due to solid state effects. Figure 4a shows EPR data of **3** obtained in toluene, along with a fit of these data. The relatively strong coupling between isolated molecules of **3** in the solid state is unusual, and likely due to a distinct amount of radical character on the phenolate rings in this complex, as suggested by DFT calculations. Figure 4b shows a spin density plot of **3**, obtained from a calculation with B3LYP/TZVP, which includes calculated spin densities on the phenolate carbons. In total, a net spin density of about |0.15| is transferred to each phenolate ring (not counting the coordinating O atoms). In this sense, complex **3** could be considered a "non-classical" hs-{FeNO}^{7} complex with multiple, redox-active ligands, although only partial oxidation of the phenolates is observed here.

The 4.2-K/53-mT Mössbauer spectrum of **3** exhibits a quadrupole doublet with $\delta = 0.56$ mm/s and $\triangle EQ = 0.92$ mm/s (Figure S32, see Table S20 for a comparison to other complexes). These parameters are in excellent agreement with those calculated by DFT (BP86 with TZVP basis set and CP(PPP) for Fe)[71] using the optimized structure, which gave an isomer shift of 0.60 mm/s and a quadrupole splitting of 1.07 mm/s. Importantly, solid state IR spectroscopy of **3** shows the N-O stretch of this complex at 1689 cm^{-1}, which shifts to 1654 cm^{-1} in the ^{15}NO analog (Figure 5). *This is one of the lowest N-O stretching*

frequencies reported so far for a mononuclear hs-FeNO}[7] complex, which supports the idea that **3** contains a highly activated (reduced) $^3NO^-$ ligand. In comparison, the N-O stretching frequency in **4** is located at 1742 cm^{-1}, in agreement with this conclusion.[67] This result is also in agreement with the DFT-calculated N-O stretch for **3**, predicted at 1699 cm^{-1} with BP86/TZVP (this method has been shown to give particularly accurate N-O stretching frequencies in previous studies on hs-{FeNO}^{7} complexes[34]). The DFT calculations also reproduce the structural features of the [FeNO] unit well, with predicted Fe-NO and N-O bond distances of 1.74 and 1.18 Å (exp: 1.79 and 1.15 Å), respectively.

To further address the unique vibrational properties of **3**, NRVS was used to measure the Fe-NO stretch of this complex, which is observed at 467 cm^{-1} (Figure 6). This band shifts to 460 cm^{-1} upon ^{15}NO labeling, confirming the assignment of this feature to the Fe-NO stretch. Previous work has shown that hs-{FeNO}^{7} complexes have hs-Fe(III)-$^3NO^-$ type electronic structures, where the $^3NO^-$ ligand acts predominantly as a strong π-donor to the hs-Fe(III) center.[62,70] This electronic structure is reflected by a direct correlation of the Fe-NO and N-O bond strengths, and hence, vibrational frequencies.[62] This is due to the fact that a reduction in π-donicity from the $^3NO^-$ ligand to the Fe(III) center, for example, weakens the Fe-NO bond and lowers the Fe-NO stretch. At the same time, due to the resulting, increased electron density in the π^* orbitals of the $^3NO^-$ ligand, the N-O bond is also weakened, which lowers the N-O stretch. Hence, this direct correlation of the Fe-NO and N-O vibrational frequencies is the hallmark of complexes with a bound $^3NO^-$ ligand. We have previously established this correlation with hs-{FeNO}^{7} complexes that feature N-O stretching frequencies in the 1720 – 1820 cm^{-1} range.[62] Complex **3** fits this analysis well and extends our correlation further into the <1700 cm^{-1} range for the N-O stretch. This observation is illustrated in Figure 7, where complex **3** is now added to the correlation line initially reported by Berto et al. in 2011.[62] Complex **3** lies on the lower end of the correlation line, due to being one of the most activated mononuclear hs-{FeNO}^{7} complexes reported to this date (see Discussion). The weak Fe-NO and N-O bonds in **3** mean that this complex has an unprecedented, large amount of unpaired electron density in its π^* orbitals, which is suitable for N-N coupling and N_2O formation. In addition, the weak Fe-NO bond in this complex further lowers the activation barrier for N-N bond formation.[34] Despite of this activation, complex **3** is stable and can be isolated, which we attribute to the fact that this complex exists exclusively in a monomeric form. In order to further confirm this hypothesis, we then investigated the NO reactivity of complex **1**, which can dimerize/oligomerize. Indeed, as discussed next, complex **1** reacts with NO to produce almost quantitative amounts of N_2O.

III.3.   Reactivity of Complex 1 with NO Gas: NO Reduction to N_2O

As discussed above, we propose that complex **3** represents a hs-{FeNO}^{7} complex that has the appropriate level of activation for direct NO reduction, but that is stabilized by the fact that it is forced to be monomeric, due to steric bulk. In order to obtain further support for this hypothesis, we then studied the reaction of complex **1** with NO, where such steric restrictions do not apply. Upon charging a round bottom flask containing a CH_2Cl_2 solution of freshly prepared complex **1** with excess NO gas, the solution immediately turned dark brown. The reaction was further monitored using UV-vis and IR spectroscopy at room

temperature. Analysis of the absorption spectra indicates that the reaction is triphasic. Upon addition of NO, there is an immediate change in the signal at 460 nm, concomitant with the appearance of a new band at 451 nm (Figure 8a). IR spectra taken <5 min after NO addition at room temperature show the formation of several different NO complexes with different degrees of activation (evident from their different N-O stretching frequencies), as shown in Figure 9, with the major signal showing the N-O stretch at 1734 cm^{-1}. The rapid formation of multiple NO complexes is then followed by slower, second and third phases of the reaction. Here, the absorption signals slowly change over the course of 24 hours, showing an isosbestic point at 484 nm, with the final product exhibiting a characteristic absorption band at 500 nm (Figures 8b and c). Solution IR data in Figure 9 show that this band forms concomitantly with the disappearance of the N-O stretching signals in the IR spectrum, and the appearance of the N-N stretch of N_2O. After 8 hours, the total N_2O yield reaches its maximum accumulation at 81%, indicating almost quantitative NO reduction by **1**, with no further subsequent change of the N_2O yield within ±5%. Solution IR data in Figure 9 (enlarged in Figure S12) show that after 24 hours, there is still a small amount of NO complexes left in solution, as indicated by the N-O stretching bands at 1750 and 1712 cm^{-1}, which likely accounts for the missing ~20% of iron-NO complexes that have not formed N_2O (yet). It is not a priori clear what the structures of these species are (likely oligomers), but they do not have the right level of activation and/or the right geometry to produce N_2O. Considering the stability and slow decay observed for the NO complexes with N-O stretching frequencies >1710 cm^{-1} in the IR data, it is clear that these remaining species are not the ones responsible for N_2O formation. Data showing N_2O yields over time are presented in Figures S19–S25.

We also monitored the reaction of **1** with NO by Mössbauer and EPR spectroscopy (Figures S1 and S3) to see the fate of the iron centers during the reaction. Comparison of the Mössbauer spectra before and after reaction of a solution of **1** with excess NO gas for 48 h shows the conversion of 62% of the quadrupole doublet associated with **1** (δ = 1.15 mm/s and ΔEQ = 2.89 mm/s) to a new quadrupole doublet with parameters (δ = 0.52 mm/s and ΔEQ = 0.88 mm/s, 30% intensity) that are characteristic of an antiferromagnetically coupled dimer of hs-Fe(III) centers, which has a diamagnetic ground state (S_t = 0). We propose that this species is likely associated with a diferric product that is formed after direct reduction of NO to N_2O, potentially an oxo-bridged diferric complex (Scheme 3; compare to the diferric product formed after NO reduction in ref. [40] with δ = 0.53 mm/s and ΔEQ = 0.80 mm/s). In addition, the broad magnetically split features of mononuclear hs-Fe(III) and hs-{FeNO}^{7} complex(es) appear in the Mössbauer spectrum. This assignment is further supported by EPR data (Figure S5), which reveal the diagnostic signals associated with rhombic hs-Fe(III) centers with S_t = 5/2 (a nearly isotropic signal at g_{eff} = 4.3) and with hs-{FeNO}^{7} centers with S_t = 3/2 (an axial signal with g_{eff} values of 4, 2).

In summary, these results demonstrate the ability of the sterically unhindered complex **1** to mediate direct NO reduction, supporting the claim that both complexes **1** and **2** have suitable electronic properties to support this reaction, and that it is simply the inability of **3** to form dimeric (or oligomeric) structures that stabilizes this activated hs-{FeNO}^{7} species. In this sense, complex **3** is an electronic model for hs-{FeNO}^{7} complexes that are activated for

direct NO reduction. This claim is further supported by the literature: whereas the dimeric complex $[Fe^{II}_2((Py_2PhO_2)MP)(OAc)_2]^-$, for example, is able to mediate fast and efficient N_2O formation, monomeric complexes like the hs-{FeNO}^{8} complex $[Fe(N3PyS)(NO)]$ can only produce N_2O over longer periods of time (54% in 20 h).[40,72] In addition, complex **1** represents only the second example of direct NO reduction by a synthetic non-heme iron model complex.

III.4. DFT Modeling of The Dimeric NO Intermediate and Mechanistic Implications

The solution IR, EPR and Mössbauer data obtained during the reaction of **1** with NO gas indicate the formation of multiple NO complexes in solution, in agreement with the plasticity of the ligand $H_2[MPA-(PhO)_2]$ (see Scheme 3). However, based on literature precedence with our dimeric complex $[Fe^{II}_2((Py_2PhO_2)MP)(OAc)_2]^-$, and the fact that the mononitrosyl complex **3** does not support NO reduction to N_2O, we propose that a diferrous dinitrosyl complex of **1**, or a corresponding motif in a larger oligomer, with the NO ligands in a cis orientation (see Scheme 3) is responsible for N_2O generation, at least on the shorter timescale. Over the course of multiple hours, we cannot rule out that some of the N_2O is produced by bimolecular reactions. In order to determine what the properties of such a species, $[\{Fe(MPA-(PhO)_2)(NO)\}_2]$, would be, and how the N-O stretching frequencies of this intermediate compare to the solution IR data, we conducted DFT calculations on the corresponding cis isomer, which is the relevant species for N_2O formation (the trans isomer can be expected to be electronically very similar, due to the identical first coordination sphere of the iron centers). For this purpose, we chose the BP86/TZVP method, which shows excellent agreement between the calculated and observed structure and N-O stretching frequency for **3**. The optimized structure of cis-$[\{Fe(MPA-(PhO)_2)(NO)\}_2]$ reveals a slightly asymmetric structural core (see Figures 10 and S45). The two hs-{FeNO}^{7} moieties are typical non-heme hs-{FeNO}^{7} centers with an Fe(III)-^{3}NO$^-$ electronic structure (S = 3/2). The two units are further antiferromagnetically coupled in the dimer to give a $S_t = 0$ ground state. Importantly, the (O)N-Fe-Fe-N(O) dihedral angle is 12°, which shows that the FeNO units are co-planar, and satisfy this important requirement for N-N coupling in FNORs.[36] These results clearly indicate that cis-$[\{Fe(MPA-(PhO)_2)(NO)\}_2]$ is the species with the right conformation to carry out direct NO reduction to N_2O in solution.

The calculated N-O stretching frequencies for cis-$[\{Fe(MPA-(PhO)_2)(NO)\}_2]$ are 1700 and 1649 cm^{-1}, which shows that this species is highly activated for NO reduction. Importantly, this result also implies that the relatively stable NO complexes observed by solution IR spectroscopy with N-O stretching frequencies in the 1730 – 1790 cm^{-1} range (see Figure 9) cannot correspond to cis-$[\{Fe(MPA-(PhO)_2)(NO)\}_2]$, the corresponding trans complex, or other, related species, as they are all expected to show N-O stretching frequencies below ~1710 cm^{-1}. In comparison, complex **4**, which contains only one phenolate group, shows the N-O stretch at 1742 cm^{-1}. This provides direct evidence that the relatively stable NO complexes observed in the reaction of **1** with NO gas in Figure 9 must correspond to complexes where at least one phenolate ligand is no longer coordinated to the iron center (indicated as "less activated" in Scheme 3). Vice versa, this lowers the activation of these complexes for NO reduction, evident from their N-O stretching frequencies in the 1730 – 1790 cm^{-1} range.

To further corroborate these results, we also geometry-optimized (BP86/TZVP) the structure of the monomeric hs-{FeNO}^{7} complex [Fe(MPA-(PhO)$_2$)(NO)] (Figure 10). The calculations reveal a structure with Fe-NO and an N-O bond distances of 1.74 and 1.18 Å, respectively, and an Fe-N-O bond angle of 142°. The N-O stretching frequency of this complex is predicted at 1712 cm^{-1}, which is very similar to the N-O stretch calculated for **3**, at 1699 cm^{-1}. This indicates that the monomeric complex [Fe(MPA-(PhO)$_2$)(NO)] has very similar electronic properties as **3**, which is the expected result, and which further indicates that the DFT calculations provide a good geometric and electronic description of the critical intermediate cis-[{Fe(MPA-(PhO)$_2$)(NO)}$_2$].

IV. Discussion

In this paper, we have demonstrated the stabilization of a highly activated mononuclear hs-{FeNO}^{7} complex, using steric protection. Here, reaction of the dimeric precursor **2** with excess NO gas produced the monomeric, stable hs-{FeNO}^{7} complex **3**. This compound has one of the lowest N-O stretching frequencies observed in a monomeric hs-{FeNO}^{7} complex to this date, at 1689 cm^{-1}. Recently, Goldberg and coworkers reported the complex [Fe(Me$_3$TACN)((OSi^{Ph2})$_2$O)(NO)] with a low N-O stretch of 1680 cm^{-1}, observed via Raman spectroscopy, indicating that this complex has a similar level of activation as complex **3** (see Table 1 and S20).[37] Correspondingly, the Fe-NO stretches in these complexes are also similar, 467 cm^{-1} in **3** (via NRVS) compared to 460 cm^{-1} in Goldberg's complex (via Raman spectroscopy). [Fe(Me$_3$TACN)((OSi^{Ph2})$_2$O)(NO)] is stable for at least 2 hours at room temperature without N$_2$O formation, while complex **3** is stable indefinitely while kept inside the inert atmosphere of the glovebox. The low energy Fe-NO stretch of **3** is in agreement with the direct correlation of the Fe-NO and N-O stretching frequencies generally observed in hs-{FeNO}^{7} complexes, which is a testimony of the dominant π-donor interaction between the ^{3}NO$^-$ ligand and the Fe(III) center in these complexes. The low N-O stretching frequency in **3** is related to a large amount of unpaired electron density in the π* orbitals of the ^{3}NO$^-$ ligand, which activates the complex for N-N bond formation and NO reduction. Hence, as we show here, _the N-O stretching frequency serves as a measure for the degree of activation of the coordinated ^{3}NO$^-$ ligand in hs-{FeNO}^{7} complexes._ Our results show that N-O stretching frequencies 1700 cm^{-1} represent the appropriate level of activation of the FeNO unit to allow for direct NO coupling to occur, leading to N$_2$O formation. This latter conclusion is further substantiated by reactivity studies on complex **1**, which is an analogue of **2** that lacks the bulky tert-butyl groups in the SCS. This complex reacts with NO gas to generate N$_2$O via the direct reduction pathway. We rationalize this difference in reactivity with the need for a dimeric structure for a model system to mediate efficient NO reduction. We propose that in the case of **1**, due to the absence of steric bulk, the complex forms a diiron dinitrosyl intermediate, cis-[{Fe^{II}(MPA-(PhO)$_2$)(NO)}$_2$], which rapidly proceeds to form N$_2$O, similar to our previous model complex, [Fe^{II}$_2$((Py$_2$PhO$_2$)MP)(OAc)$_2$]$^-$. However, due to the lack of proper preorganization of the iron centers with open cis coordination sites, as in [Fe^{II}$_2$((Py$_2$PhO$_2$)MP)(OPr)$_2$]$^-$, NO reduction by **1** is (a) much slower, and produces 81% N$_2$O over 8 hours, and (b) much less efficient, with the formation of multiple NO complexes, the majority of which is not activated for NO reduction. Nevertheless, this makes complex **1** only the second model complex reported

in the literature that is capable of directly reducing NO to N_2O. It is worth noting that the addition of water into a solution of complex $[Fe(Me_3TACN)((OSi^{Ph2})_2O)(NO)]$ in THF (10:1 THF:H_2O) causes immediate decay of this complex to form N_2O with 30% yield, based on a 2:1 (Fe complex):N_2O ratio, and unidentified iron products. Thus, in this case an excess amount of a proton source is required for the generation of N_2O, but the actual intermediate that forms after water addition and that is ultimately responsible for N_2O formation was not identified.[37] This is in stark contrast to our observation of N_2O formation from the direct reaction of complex **1** with NO gas, which shows a close to quantitative yield of N_2O in the absence of a proton source at room temperature.

Based on our experimental and theoretical results, we hypothesize that upon reaction of **1** with NO gas in solution, both cis- and trans-$[\{Fe(MPA-(PhO)_2)(NO)\}_2]$ complexes form, where the cis isomer goes on to rapidly produce N_2O, corresponding to the initial boost in N_2O yield (38% after 15 minutes). This first phase is followed by isomerization of the trans isomer to other NO complexes that are not activated for direct NO reduction, evident from their N-O stretching frequencies >1710 cm^{-1}. Over time, some of these compounds eventually reform cis-$[\{Fe(MPA-(PhO)_2)(NO)\}_2]$ or related oligomers, which explains the slow formation of additional N_2O over 8 hours reaction time. This mechanistic scenario is summarized in Scheme 3.

Through both this study and the previous study on the dimeric complex $[Fe^{II}_2((Py_2PhO_2)MP)(OAc)_2]^-$,[40] we have now demonstrated that model complexes can indeed reduce NO directly to N_2O by tuning the reduction potential of the diiron core to activate the hs-$\{FeNO\}^7$ moieties for N-N coupling. These complexes are characterized by N-O stretching frequencies 1700 cm^{-1}. However, it is important to note that the hs-$\{FeNO\}^7$ moieties of FNORs are not as activated as these model systems, exemplified by their N-O stretching frequencies in the 1740–1750 cm^{-1} range (see Table 1 and S20).[73] How do the enzymes accomplish direct N-N coupling at this reduced driving force with less electron-rich iron centers? This finding points to the critical importance of the SCS in the active sites of FNORs. In accordance with this conclusion, experimental studies on *Tm* FDP have shown that removal of SCS residues in the active site of FNORs, especially a key tyrosine residue, retards catalysis.[74] In these variants, the NO complexes do form, but cannot proceed towards N-N coupling and N_2O formation, indicating the importance of the SCS to induce N-N bond formation in the enzymes, where the hs-$\{FeNO\}^7$ units themselves are less activated. Accordingly, recent computational studies indicate that hydrogen bonding to one of the coordinated NO ligands in the $[hs-\{FeNO\}^7]_2$ intermediate of FNORs greatly lowers the barrier for N-N bond formation.[75] In this sense, the SCS allows the enzymes to utilize less driving force (less electron-rich iron centers) to mediate direct NO reduction to N_2O compared to the model systems. Further studies are now dedicated to more thoroughly explore the role of SCS residues, especially hydrogen bond donors, for NO reduction in FNORs.

Supplementary Material

Refer to Web version on PubMed Central for supplementary material.

ACKNOWLEDGMENT:

Reference:

1. Lehnert N; Kim E; Dong HT; Harland JB; Hunt AP; Manickas EC; Oakley KM; Pham J; Reed GC; Alfaro VS The Biologically Relevant Coordination Chemistry of Iron and Nitric Oxide: Electronic Structure and Reactivity. Chem. Rev 2021, 121, 14682-14905. [PubMed: 34902255]

2. Lehnert N; Berto TC; Galinato MGI; Goodrich LE In The Role of Heme-Nitrosyls in the Biosynthesis, Transport, Sensing, and Detoxification of Nitric Oxide (NO) in Biological Systems: Enzymes and Model Complexes; Kadish KM, Smith KM, Guilard R, Eds.; World Scientific: New Jersey, 2011; Vol. 14,, p 1-247

3. Ignarro L Nitric Oxide: Biology and Pathobiology; Academic Press: San Diego, 2000.

4. Wink DA; Mitchell JB Chemical biology of nitric oxide: insights into regulatory, cytotoxic, and cytoprotective mechanisms of nitric oxide. Free Rad. Biol. Med 1998, 25, 434-456. [PubMed: 9741580]

5. Stuehr DJ; Gross SS; Sakuma I; Levi R; Nathan CF Activated Murine Macrophages Secrete a Metabolite of Arginine with the Bioactivity of Endothelium-Derived Relaxing Factor and the Chemical Reactivity of Nitric Oxide. J. Exp. Med 1989, 169, 1011-1020. [PubMed: 2784476]

6. Bogdan C Nitric oxide and the immune response. Nat. Immunol 2001, 2, 907-916. [PubMed: 11577346]

7. Gardner AM; Gessner CR; Gardner PR Regulation of the Nitric Oxide Reduction Operon (norRVW) in Escherichia coli. Role of NorR and s54 in the Nitric Oxide Stress Response. J. Biol. Chem 2003, 278, 10081-10086. [PubMed: 12529359]

8. Missall TA; Lodge JK; McEwen JE Mechanisms of Resistance to Oxidative and Nitrosative Stress: Implications for Fungal Survival in Mammalian Hosts. Eucaryot. Cell 2004, 3, 835-846.

9. Sarti P; Fiori PL; Forte E; Rappelli P; Teixeira M; Mastronicola D; Sanciu G; Giuffré A; Brunori M *Trichomonas vaginalis* degrades nitric oxide and expresses a flavorubredoxin-like protein: a new pathogenic mechanism? Cell. Mol. Life Sci 2004, 61, 618-623. [PubMed: 15004700]

10. Frazão C; Silva G; Gomes CM; Matias P; Coelho R; Sieker L; Macedo S; Liu MY; Oliveira S; Teixeira M; Xavier AV; Rodrigues-Pousada C; Carrondo MA; Le Gall J Structure of a dioxygen reduction enzyme from *Desulfovibrio gigas*. Nat. Struct. Biol 2000, 7, 1041-1045. [PubMed: 11062560]

11. Silaghi-Dumitrescu R; Kurtz DM Jr.; Ljungdahl LG; Lanzilotta WN X-ray Crystal Structures of *Moorella thermoacetica* FprA. Novel Diiron Site Structure and Mechanistic Insights into a Scavenging Nitric Oxide Reductase. Biochemistry 2005, 44, 6492-6501. [PubMed: 15850383]

12. Mills PC; Rowley G; Spiro S; Hinton JCD; Richardson DJ A combination of cytochrome c nitrite reductase (NrfA) and flavorubredoxin (NorV) protects Salmonella enterica serovar Typhimurium against killing by NO in anoxic environments. Microbiology 2008, 154, 1218-1228. [PubMed: 18375814]

13. Gomes CM; Giuffrè A; Forte E; Vicente JB; Saraiva LM; Brunori M; Teixeira M A Novel Type of Nitric-oxide Reductase. *Escherichia Coli* Flavorubredoxin. J. Biol. Chem 2002, 277, 25273-25276. [PubMed: 12101220]

14. Anstey NM; Weinberg JB; Hassanali MY; Mwaikambo ED; Manyenga D; Misukonis MA; Arnelle DR; Hollis D; McDonald MI; Granger DL Nitric oxide in Tanzanian children with malaria: inverse

relationship between malaria severity and nitric oxide production/nitric oxide synthase type 2 expression. J. Exp. Med 1996, 184, 557-567. [PubMed: 8760809]

15. Evans TG; Thai L; Granger DL; Hibbs JB Effect of in vivo inhibition of nitric oxide production in murine leishmaniasis. J. Immunol 1993, 151, 907. [PubMed: 8335918]

16. Stenger S; Donhauser N; Thüring H; Röllinghoff M; Bogdan C Reactivation of latent leishmaniasis by inhibition of inducible nitric oxide synthase. J. Exp. Med 1996, 183, 1501-1514. [PubMed: 8666908]

17. Nicholson S; Bonecini-Almeida M. d. G.; Lapa e Silva JR; Nathan C; Xie QW; Mumford R; Weidner JR; Calaycay J; Geng J; Boechat N; Linhares C; Rom W; Ho JL Inducible nitric oxide synthase in pulmonary alveolar macrophages from patients with tuberculosis. J. Exp. Med 1996, 183, 2293-2302. [PubMed: 8642338]

18. Privett BJ; Broadnax AD; Bauman SJ; Riccio DA; Schoenfisch MH Examination of bacterial resistance to exogenous nitric oxide. Nitric Oxide 2012, 26, 169-173. [PubMed: 22349019]

19. Hoehn T; Huebner J; Paboura E; Krause M; Leititis JU Effect of therapeutic concentrations of nitric oxide on bacterial growth in vitro. Crit. Care Med 1998, 26, 1857-1862. [PubMed: 9824079]

20. Namivandi-Zangeneh R; Sadrearhami Z; Bagheri A; Sauvage-Nguyen M; Ho KKK; Kumar N; Wong EHH; Boyer C Nitric Oxide-Loaded Antimicrobial Polymer for the Synergistic Eradication of Bacterial Biofilm. ACS Macro Lett 2018, 7, 592-597. [PubMed: 35632937]

21. Wu Y; Deng G; Jiang K; Wang H; Song Z; Han H Photothermally triggered nitric oxide nanogenerator targeting type IV pili for precise therapy of bacterial infections. Biomaterials 2021, 268, 120588. [PubMed: 33307370]

22. Carpenter AW; Schoenfisch MH Nitric oxide release: Part II. Therapeutic applications. Chem. Soc. Rev 2012, 41, 3742-3752. [PubMed: 22362384]

23. Lehnert N; Fujisawa K; Camarena S; Dong HT; White CJ Activation of Non-Heme Iron-Nitrosyl Complexes: Turning up the Heat. ACS Catal 2019, 9, 10499-10518.

24. Pal N; Jana M; Majumdar A Reduction of NO by diiron complexes in relation to flavodiiron nitric oxide reductases. Chem. Commun 2021, 57, 8682-8698.

25. Kurtz DM Jr. Flavo-Diiron Enzymes: Nitric Oxide or Dioxygen Reductases? Dalton Trans 2007, 4115-4121.

26. Hayashi T; Caranto JD; Wampler DA; Kurtz DM Jr.; Moënne-Loccoz P Insights into the Nitric Oxide Reductase Mechanism of Flavodiiron Proteins from a Flavin-Free Enzyme. Biochemistry 2010, 49, 7040–7049. [PubMed: 20669924]

27. Enemark JH; Feltham RD Principles of Structure, Bonding, and Reactivity for Metal Nitrosyl Complexes. Coord. Chem. Rev 1974, 13, 339-406.

28. Caranto JD; Weitz A; Giri N; Hendrich MP; Kurtz DM Jr. . A Diferrous-Dinitrosyl Intermediate in the N_2O-Generating Pathway of a Deflavinated Flavo-Diiron Protein. Biochemistry 2014, 53, 5631–5637. [PubMed: 25144650]

29. Caranto JD; Weitz A; Hendrich MP; Kurtz DM Jr. The Nitric Oxide Reductase Mechanism of a Flavo-Diiron Protein: Identification of Active-Site Intermediates and Products. J. Am. Chem. Soc 2014, 136, 7981–7992. [PubMed: 24828196]

30. Hayashi T; Caranto JD; Matsumura H; Kurtz DM Jr.; Moënne-Loccoz P Vibrational Analysis of Mononitrosyl Complexes in Hemerythrin and Flavodiiron Proteins: Relevance to Detoxifying NO Reductase. J. Am. Chem. Soc 2012, 134, 6878-6884. [PubMed: 22449095]

31. Jana M; Pal N; White CJ; Kupper C; Meyer F; Lehnert N; Majumdar A Functional Mononitrosyl Diiron(II) Complex Mediates the Reduction of NO to N2O with Relevance for Flavodiiron NO Reductases. J. Am. Chem. Soc 2017, 140, 14380-14383.

32. Jana M; White CJ; Pal N; Demeshko S; Meyer F; Lehnert N; Majumdar A Functional Models for the Mono- and Dinitrosyl Intermediates of FNORs: Semireduction versus Superreduction of NO. J. Am. Chem. Soc 2020, 142, 6600-6616. [PubMed: 32167756]

33. White CJ; Speelman AL; Kupper C; Demeshko S; Meyer F; Shanahan JP; Alp EE; Hu M; Zhao J; Lehnert N The Semireduced Mechanism for Nitric Oxide Reduction by Non-Heme Diiron Complexes: Modeling Flavodiiron Nitric Oxide Reductases. J. Am. Chem. Soc 2018, 140, 2562-2574. [PubMed: 29350921]

34. Van Stappen C; Lehnert N Mechanism of N-N Bond Formation by Transition Metal-Nitrosyl Complexes: Modeling Flavodiiron Nitric Oxide Reductases. Inorg. Chem 2018, 57, 4252-4269. [PubMed: 29608298]

35. Kindermann N; Schober A; Demeshko S; Lehnert N; Meyer F Reductive Transformations of a Pyrazolate-Based Bioinspired Diiron–Dinitrosyl Complex. Inorg. Chem 2016, 55, 11538-11550. [PubMed: 27788000]

36. White CJ; Lengel MO; Bracken AJ; Kampf JW; Speelman AL; Alp EE; Hu MY; Zhao J; Lehnert N Distortion of the [FeNO]2 Core in Flavodiiron Nitric Oxide Reductase Models Inhibits N–N Bond Formation and Promotes Formation of Unusual Dinitrosyl Iron Complexes: Implications for Catalysis and Reactivity. J. Am. Chem. Soc 2022, 144, 3804-3820. [PubMed: 35212523]

37. Dey A; Gordon JB; Albert T; Sabuncu S; Siegler MA; MacMillan SN; Lancaster KM; Moënne-Loccoz P; Goldberg DP A Nonheme Mononuclear {FeNO}7 Complex that Produces N2O in the Absence of an Exogenous Reductant. Angew. Chem. Int. Ed 2021, 60, 21558-21564.

38. Zheng S; Berto TC; Dahl EW; Hoffman MB; Speelman AL; Lehnert N The Functional Model Complex [Fe$_2$(BPMP)(OPr)(NO)$_2$](BPh$_4$)$_2$ Provides Insight into the Mechanism of Flavodiiron NO Reductases. J. Am. Chem. Soc 2013, 135, 4902–4905. [PubMed: 23472831]

39. Jiang Y; Hayashi T; Matsumura H; Do LH; Majumdar A; Lippard SJ; Moënne-Loccoz P Light-Induced N$_2$O Production from a Non-heme Iron–Nitrosyl Dimer. J. Am. Chem. Soc 2014, 136, 12524-12527. [PubMed: 25158917]

40. Dong HT; White CJ; Zhang B; Krebs C; Lehnert N Non-Heme Diiron Model Complexes Can Mediate Direct NO Reduction: Mechanistic Insight into Flavodiiron NO Reductases. J. Am. Chem. Soc 2018, 140, 13429-13440. [PubMed: 30220202]

41. Dahl EW; Dong HT; Szymczak NK Phenylamino derivatives of tris(2-pyridylmethyl)amine: hydrogen-bonded peroxodicopper complexes. Chem. Commun 2018, 54, 892-895.

42. Fujisawa K; Soma S; Kurihara H; Dong HT; Bilodeau M; Lehnert N A Cobalt-Nitrosyl Complex with a Hindered Hydrotris(pyrazolyl)borate Coligand: Detailed Electronic Structure, and Reactivity towards Dioxygen. Dalton Trans 2017, 46, 13273-13289. [PubMed: 28749492]

43. Fujisawa K; Soma S; Kurihara H; Ohta A; Dong HT; Minakawa Y; Zhao J; Alp EE; Hu MY; Lehnert N Stable Ferrous Mononitroxyl {FeNO}[8] Complex with a Hindered Hydrotris(pyrazolyl)borate Coligand: Structure, Spectroscopic Characterization, and Reactivity Toward NO and O$_2$. Inorg. Chem 2019, 58, 4059-4062. [PubMed: 30864791]

44. MacBeth CE; Golombek AP; Young VG; Yang C; Kuczera K; Hendrich MP; Borovik AS O$_2$ Activation by Nonheme Iron Complexes: A Monomeric Fe(III)-Oxo Complex Derived From O$_2$. Science 2000, 289, 938. [PubMed: 10937994]

45. Yandulov DV; Schrock RR Catalytic Reduction of Dinitrogen to Ammonia at a Single Molybdenum Center. Science 2003, 301, 76. [PubMed: 12843387]

46. England J; Guo Y; Farquhar ER; Young VG Jr.; Münck E; Que L Jr. The Crystal Structure of a High-Spin Oxoiron(IV) Complex and Characterization of Its Self-Decay Pathway. J. Am. Chem. Soc 2010, 132, 8635-8644. [PubMed: 20568768]

47. Kitajima N; Fujisawa K; Morooka Y Tetrahedral Copper(II) Complexes Supported by a Hindered Pyrazolylborate. Formation of the Thiolato Complex, Which Closely Mimics the Spectroscopic Characteristics of Blue Copper Proteins. J. Am. Chem. Soc 1990, 112, 3210-3212.

48. Collman JP; Gagne RR; Reed CA; Halbert TR; Lang G; Robinson WT Picket fence porphyrins. Synthetic models for oxygen binding hemoproteins J. Am. Chem. Soc 1975, 97, 1427-1439. [PubMed: 1133392]

49. Fujisawa K; Tanaka M; Moro-oka Y; Kitajima N A Monomeric Side-On Superoxocopper(II) Complex: Cu(O$_2$)(HB(3-tBu-5-iPrpz)$_3$). J. Am. Chem. Soc 1994, 116, 12079-12080.

50. Zurita D; Scheer C; Pierre J-L; Saint-Aman E Solution studies of copper(II) complexes as models for the active site in galactose oxidase. Dalton Trans 1996, 4331-4336.

51. Tang L-Z; Lin C-N; Zhan S-Z Effect of ligand modification on hydrogen production catalyzed by iron(III) complexes supported by amine-bis(phenolate) ligands. Polyhedron 2016, 110, 247-253.

52. Lehnert N; Galinato MGI; Paulat F; Richter-Addo GB; Sturhahn W; Xu N; Zhao J Nuclear Resonance Vibrational Spectroscopy applied to [Fe(OEP)(NO)]: the Vibrational Assignments of

Five-Coordinate Ferrous Heme Nitrosyls and Implications for Electronic Structure. Inorg. Chem 2010, 49, 4133-4148. [PubMed: 20345089]

53. Sage JT; Paxson C; Wyllie GRA; Sturhahn W; Durbin SM; Champion PM; Alp EE; Scheidt WR Nuclear resonance vibrational spectroscopy of a protein active-site mimic. J. Phys. Condens. Matter 2001, 13, 7707-7722.

54. Sturhahn W Nuclear resonant spectroscopy. J. Phys. Condens. Matter 2004, 16, S497-S530.

55. Frisch MJ; Trucks GW; Schlegel HB; Scuseria GE; Robb MA; Cheeseman JR; Scalmani G; Barone V; Mennucci B; Petersson GA; Nakatsuji H; Caricato M; Li X; Hratchian HP; Izmaylov AF; Bloino J; Zheng G; Sonnenberg JL; Hada M; Ehara M; Toyota K; Fukuda R; Hasegawa J; Ishida M; Nakajima T; Honda Y; Kitao O; Nakai H; Vreven T; Montgomery JA; Peralta JE; Ogliaro F; Bearpark M; Heyd JJ; Brothers E; Kudin KN; Staroverov VN; Kobayashi R; Normand J; Raghavachari K; Rendell A; Burant JC; Iyengar SS; Tomasi J; Cossi M; Rega N; Millam JM; Klene M; Knox JE; Cross JB; Bakken V; Adamo C; Jaramillo J; Gomperts R; Stratmann RE; Yazyev O; Austin AJ; Cammi R; Pomelli C; Ochterski JW; Martin RL; Morokuma K; Zakrzewski VG; Voth GA; Salvador P; Dannenberg JJ; Dapprich S; Daniels AD; Farkas; Foresman JB; Ortiz JV; Cioslowski J; Fox DJ. Gaussian 09, Revision B.01. Wallingford CT 2009.

56. Neese F Software update: the ORCA program system, version 4.0 Released in 2018.

57. White CJ; Speelman AL; Kupper C; Demeshko S; Meyer F; Shanahan JP; Alp EE; Hu M; Zhao J; Lehnert N The Semireduced Mechanism for Nitric Oxide Reduction by Non-Heme Diiron Complexes: Modeling Flavodiiron NO Reductases. J. Am. Chem. Soc 2018, 140, 2562-2574. [PubMed: 29350921]

58. Münck E In Physical Methods in Bioinorganic Chemistry; Que L Jr, Ed.; University Science Books: Sausalito, CA, 2000, p 287-319.

59. Nakashige TG; Zhang B; Krebs C; Nolan EM Human calprotectin is an iron-sequestering host-defense protein. Nat. Chem. Bio 2015, 11, 765-771. [PubMed: 26302479]

60. Heidari S; Safaei E; Wojtczak A; Coti P; Kozakiewicz A Iron(III) complexes of pyridine-based tetradentate aminophenol ligands as structural model complexes for the catechol-bound intermediate of catechol dioxygenases. Polyhedron 2013, 55, 109-116.

61. Hasan K; Fowler C; Kwong P; Crane AK; Collins JL; Kozak CM Synthesis and structure of iron(iii) diamine-bis(phenolate) complexes. Dalton Trans 2008, 2991-2998. [PubMed: 18493635]

62. Berto TC; Hoffman MB; Murata Y; Landenberger KB; Alp EE; Zhao J; Lehnert N Structural and Electronic Characterization of Non-Heme Fe(II)-Nitrosyls as Biomimetic Models of the FeB Center of Bacterial Nitric Oxide Reductase (NorBC). J. Am. Chem. Soc 2011, 133, 16714–16717. [PubMed: 21630658]

63. Taft KL; Delfs CD; Papaefthymiou GC; Foner S; Gatteschi D; Lippard SJ [Fe(OMe)$_2$(O$_2$CCH$_2$Cl)]10, a Molecular Ferric Wheel. J. Am. Chem. Soc 1994, 116, 823-832.

64. Taft KL; Lippard SJ Synthesis and structure of [Fe(OMe)$_2$(O$_2$CCH$_2$Cl)]10: a molecular ferric wheel. J. Am. Chem. Soc 1990, 112, 9629-9630.

65. Sydora OL; Wolczanski PT; Lobkovsky EB Ferrous Wheels, Ellipse [(tBu$_3$SiS)FeX]$_n$, and Cube [(tBu$_3$SiS)Fe(CCSitBu$_3$)]$_4$. Angew. Chem. Int. Ed 2003, 42, 2685-2687.

66. Sushila; Dhamija S; Patra M; Pécaut J; Kataria R; Goswami S; Bhowmik S; Patra R Probing the structural features and magnetic behaviors in dinuclear cobalt(II) and trinuclear iron(III) complexes. Inorg. Chim. Acta 2022, 535, 120852.

67. Dong HT; Speelman AL; Kozemchak CE; Sil D; Krebs C; Lehnert N The Fe$_2$(NO)$_2$ Diamond Core: A Unique Structural Motif in Non-Heme Iron-NO Chemistry. Angew. Chem. Int. Ed 2019, 131, 17859-17863.

68. Speelman AL; White CJ; Zhang B; Alp EE; Zhao J; Hu M; Krebs C; Penner-Hahn J; Lehnert N Non-heme High-Spin {FeNO}[6-8] Complexes: One Ligand Platform Can Do It All. J. Am. Chem. Soc 2018, 140, 11341-11359. [PubMed: 30107126]

69. Li J; Banerjee A; Pawlak PL; Brennessel WW; Chavez FA Highest Recorded N–O Stretching Frequency for 6-Coordinate {Fe-NO}[7] Complexes: An Iron Nitrosyl Model for His$_3$ Active Sites. Inorg. Chem 2014, 53, 5414-5416. [PubMed: 24840527]

70. Brown CA; Pavlosky MA; Westre TE; Zhang Y; Hedman B; Hodgson KO; Solomon EI Spectroscopic and Theoretical Description of the Electronic Structure of S = 3/2 Iron-Nitrosyl

Complexes and Their Relation to O_2 Activation by Non-Heme Iron Enzyme Active Sites J. Am. Chem. Soc 1995, 117, 715-732.

71. Römelt M; Ye S; Neese F Calibration of Modern Density Functional Theory Methods for the Prediction of 57Fe Mössbauer Isomer Shifts: Meta-GGA and Double-Hybrid Functionals. Inorg. Chem 2009, 48, 784-785. [PubMed: 19102678]

72. Confer AM; McQuilken AC; Matsumura H; Moënne-Loccoz P; Goldberg DP A Nonheme, High-Spin {FeNO}[8] Complex that Spontaneously Generates N_2O. J. Am. Chem. Soc 2017, 139, 10621-10624. [PubMed: 28749673]

73. Berto TC; Speelman A; Zheng S; Lehnert N Mono- and Dinuclear Non-Heme Iron-Nitrosyl Complexes: Models for Key Intermediates in Bacterial Nitric Oxide Reductases. Coord. Chem. Rev 2013, 257, 244-259.

74. Biswas S; Kurtz DM; Montoya SR; Hendrich MP; Bominaar EL The Catalytic Role of a Conserved Tyrosine in Nitric Oxide-Reducing Non-heme Diiron Enzymes. ACS Catal 2020, 10, 8177-8186.

75. Lu J; Bi B; Lai W; Chen H Origin of Nitric Oxide Reduction Activity in Flavo-Diiron NO Reductase: Key Roles of the Second Coordination Sphere. Angew. Chem. Int. Ed 2019, 58, 3795-3799.

76. Keilwerth M; Hohenberger J; Heinemann FW; Sutter J; Scheurer A; Fang H; Bill E; Neese F; Ye S; Meyer K A Series of Iron Nitrosyl Complexes {Fe–NO}[6–9] and a Fleeting {Fe–NO}[10] Intermediate en Route to a Metalacyclic Iron Nitrosoalkane. J. Am. Chem. Soc 2019, 141, 17217-17235. [PubMed: 31566964]
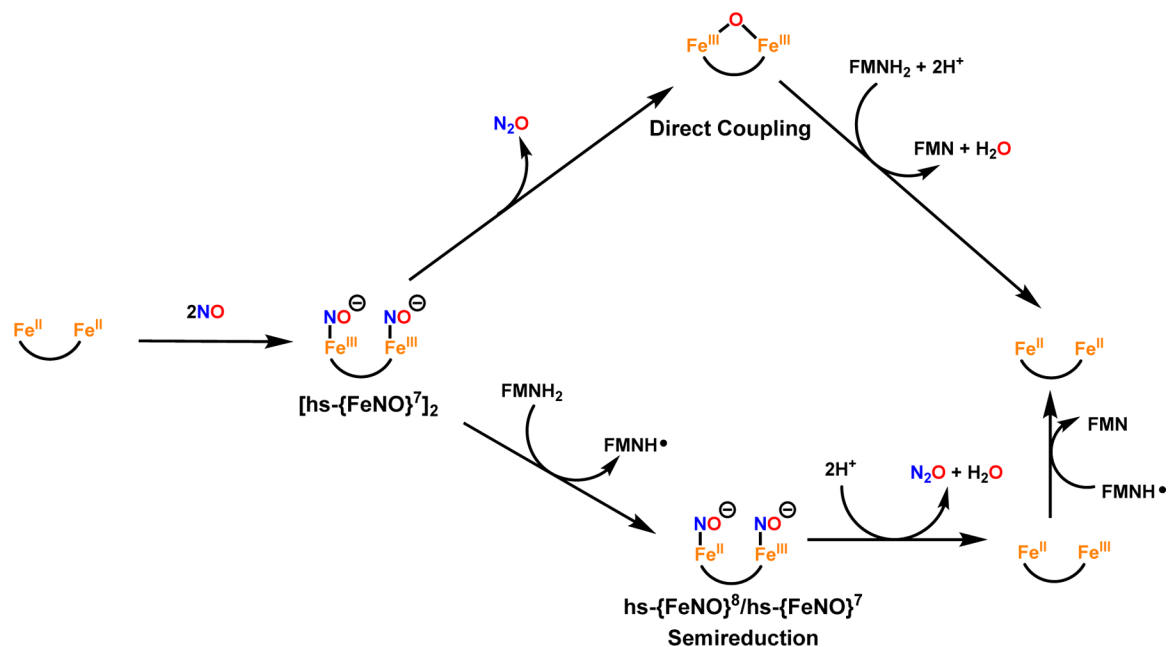
Scheme 1.
Direct NO reduction (top) and semireduction mechanisms (bottom) for the reduction of NO to N_2O, which have been demonstrated in FNORs and suitable diiron model complexes.
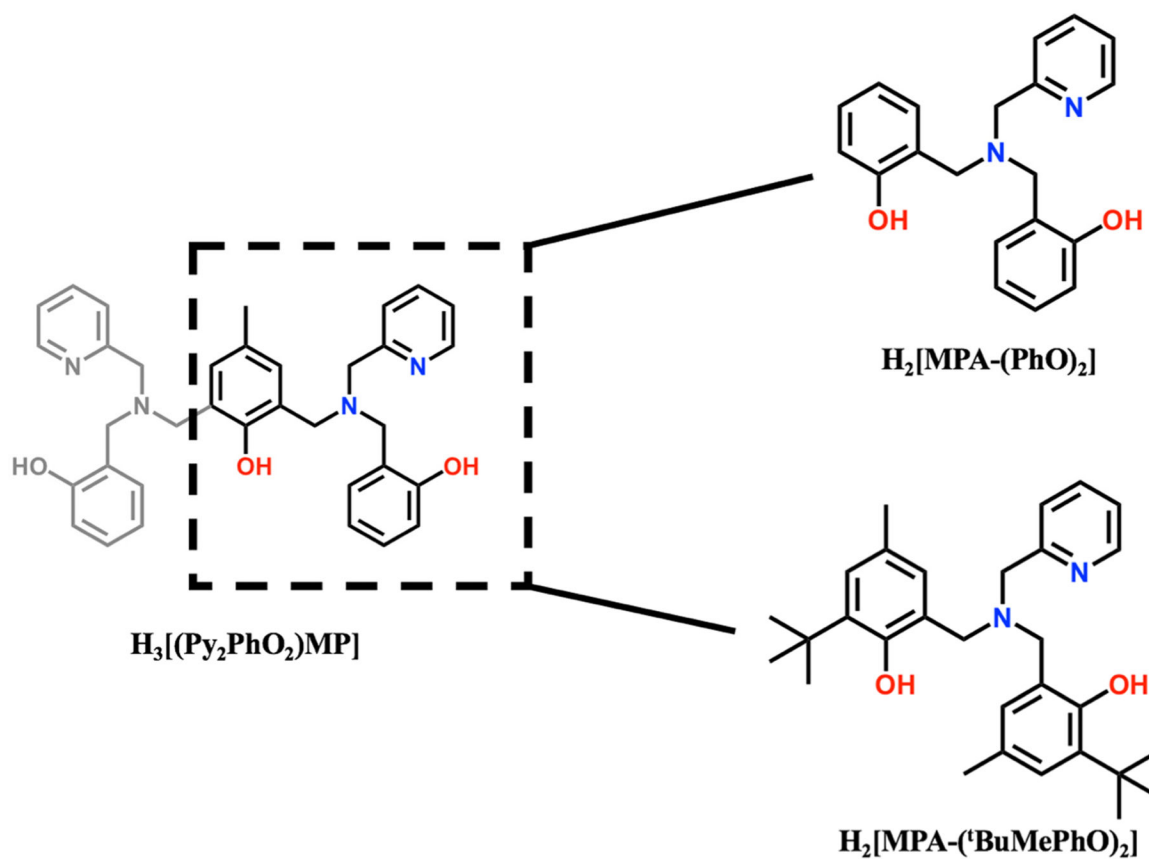
Scheme 2.
The ligands $H_2[MPA-(^tBuMePhO)_2]$ and $H_2[MPA-(PhO)_2]$ with primary coordination spheres similar to half of the ligand $H_3[(Py2PhO_2)MP]$ were chosen for this study.
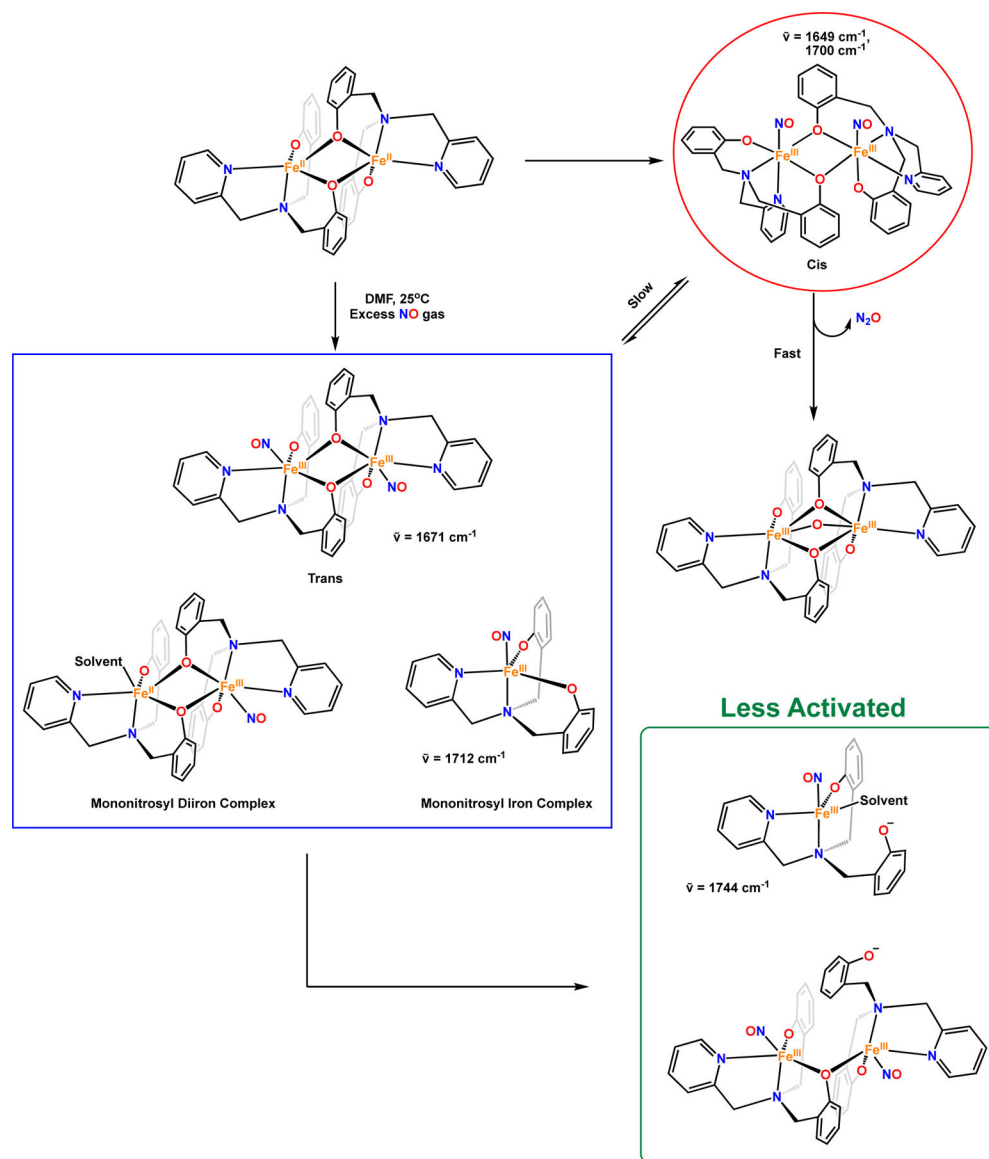
Scheme 3.
Reaction pathway of complex **1** with NO gas and proposed species present in solution (in addition to possible oligomers) based on spectroscopic analysis. The "cis" complex has an (O)N-Fe-Fe-N(O) dihedral angle around 0°, whereas in the "trans" compound the angle is ~180°. The final (main) product, an oxo-bridged diferric complex (and small amounts of unreacted, less activated nitrosyl complexes), is suggested by Mössbauer and IR spectroscopy. Calculated N-O stretching frequencies (BP86/TZVP) for select species are indicated.
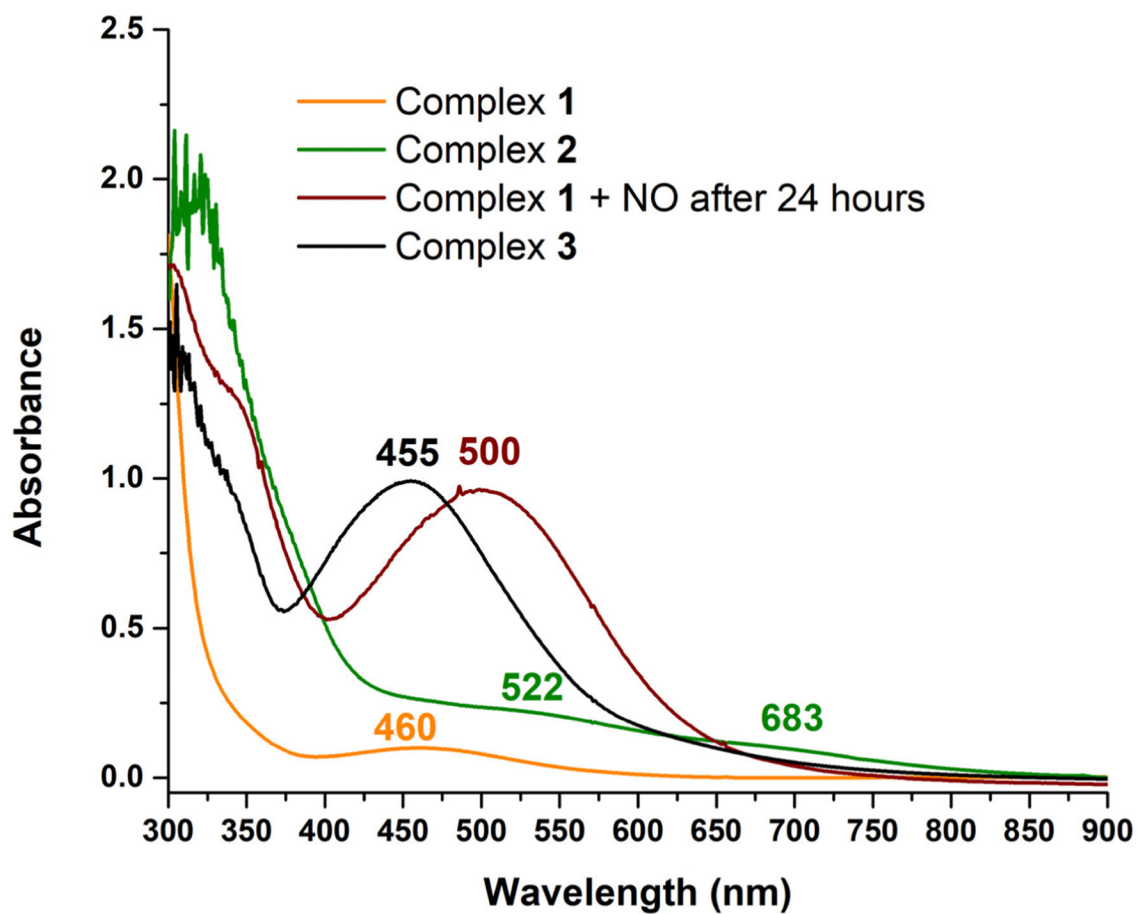
Figure 1.
UV-Vis absorption spectra of complexes [{Fe^{II}(MPA-(PhO)$_2$)}$_2$] (**1**), [{Fe^{II}(MPA-(^{t}BuMePhO)$_2$)}$_2$] (**2**), **3**, and of the product of the reaction of complex **1** with NO gas (after 24 hours), all collected in CH$_2$Cl$_2$ solution at room temperature.
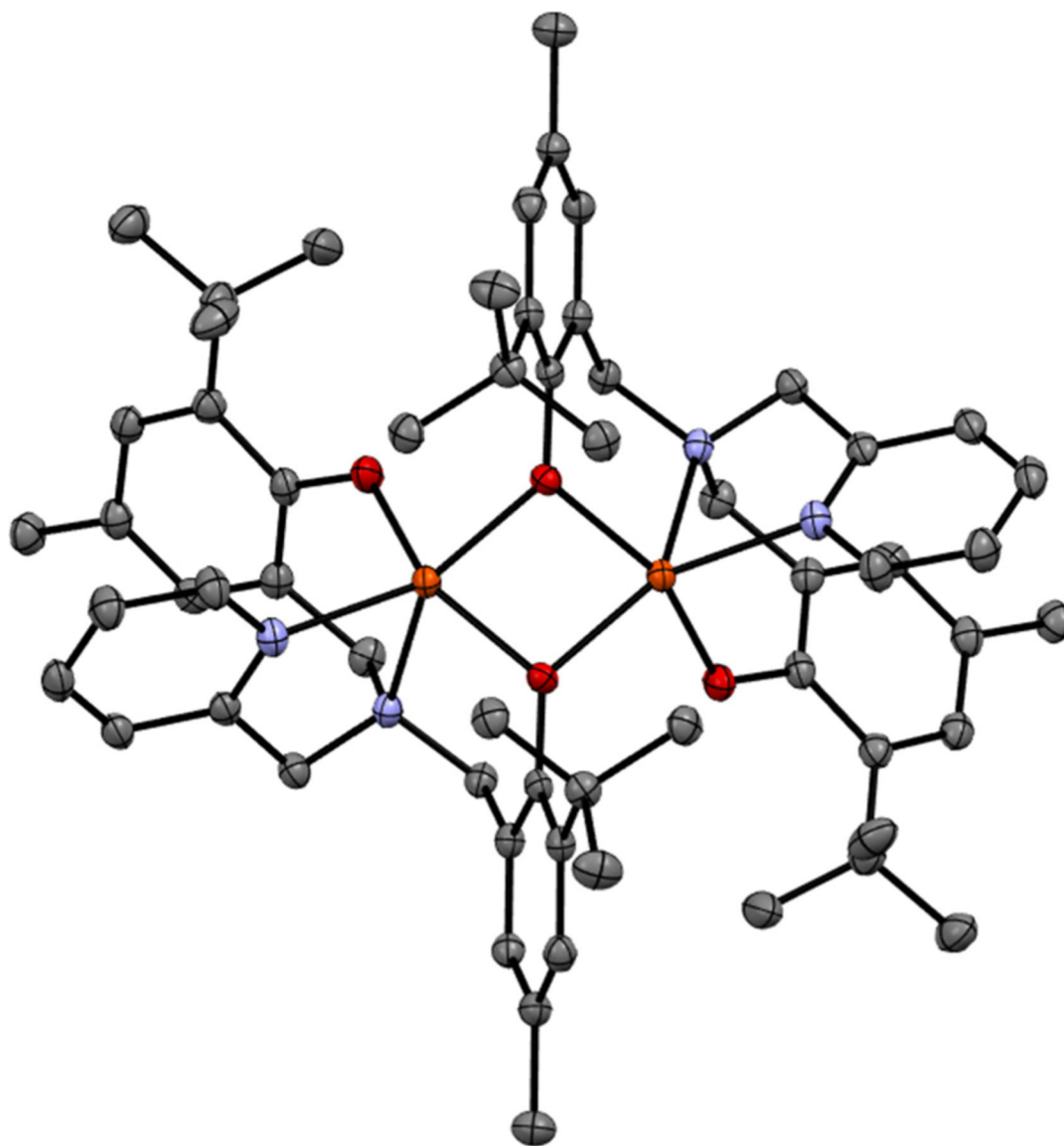
Figure 2.
Crystal structure of complex **2** with ellipsoids drawn at 50% probability. Solvent molecules
(CH_2Cl_2) and hydrogen atoms are omitted for clarity.
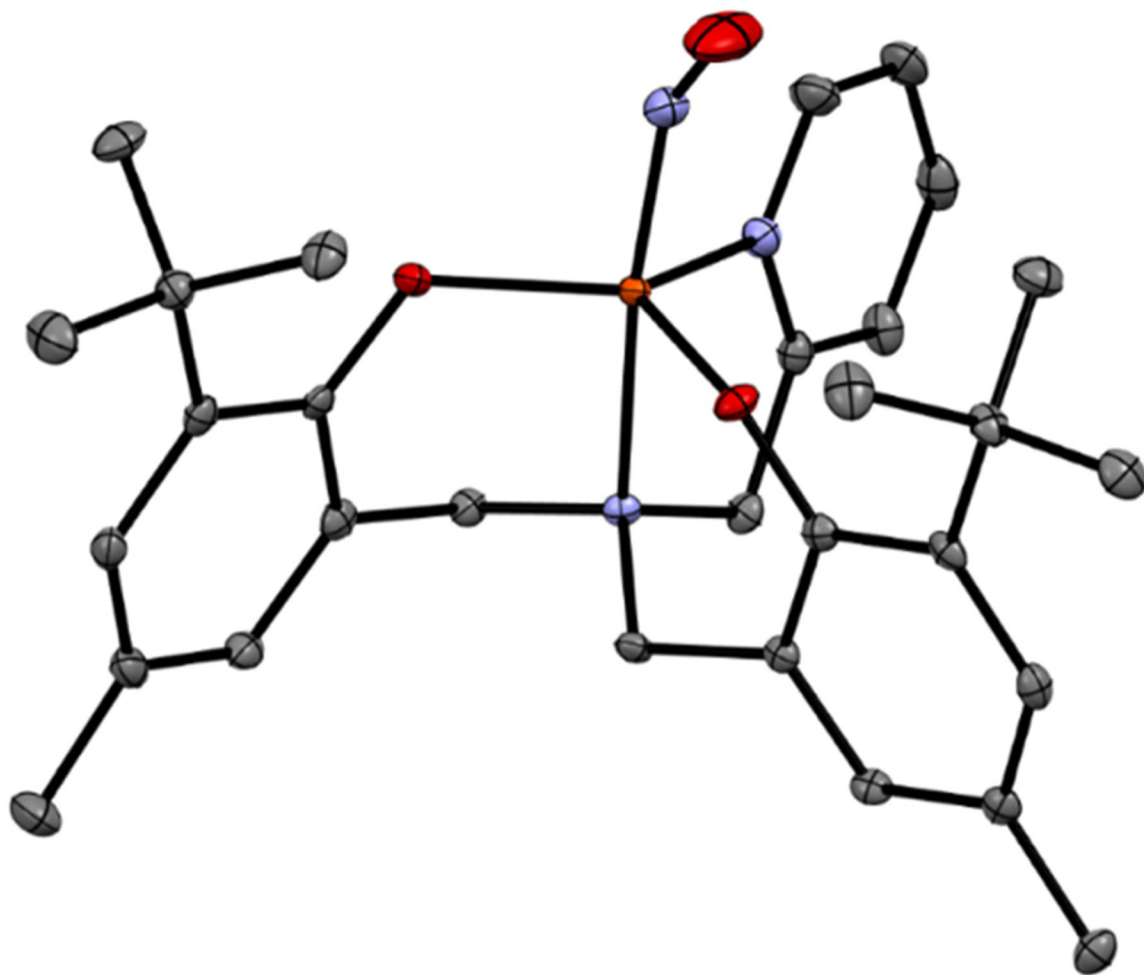
Figure 3.
Crystal structure of complex **3** with ellipsoids drawn at 50% probability. Hydrogen atoms are omitted for clarity.
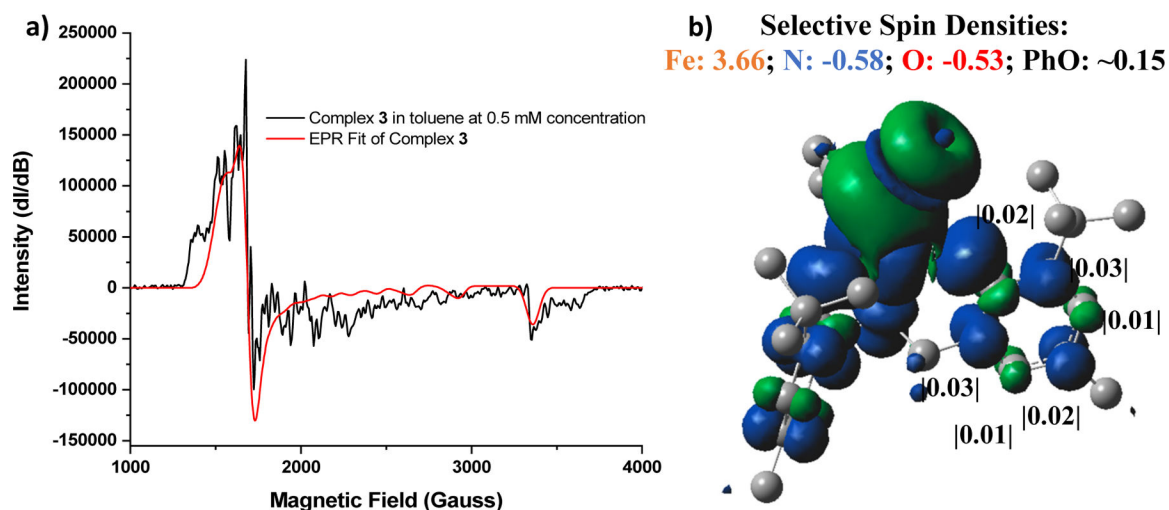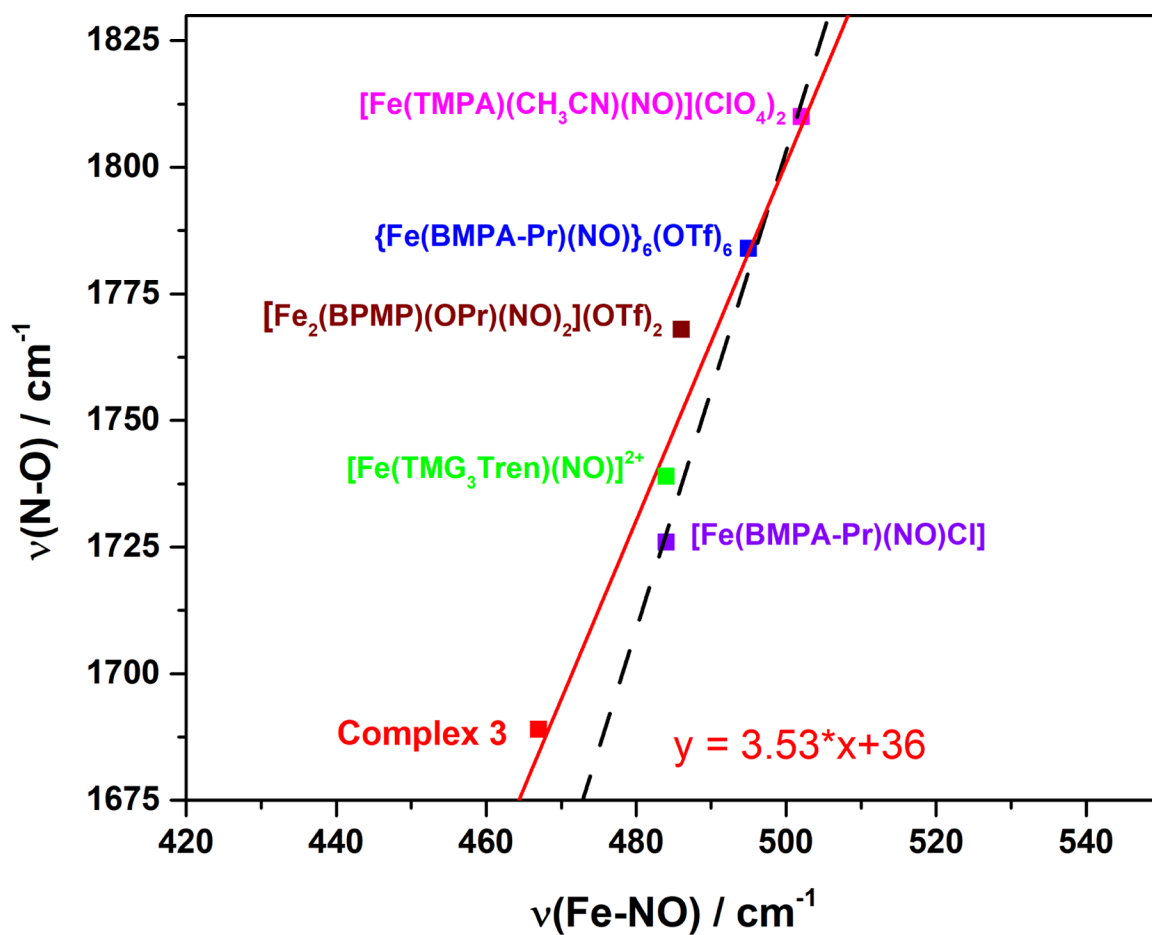
Figure 4.

a) X-band EPR spectrum of complex **3** (black line) in toluene at 0.5 mM concentration, showing signals at $g_{eff} = 4, 2$, typical for an $S_{tot} = 3/2$ hs-{FeNO}[7] complex, with additional splittings due to solid state effects. The EPR spectrum was collected at 4 K using ~20 mW microwave power and 100 kHz field modulation with the amplitude set to 1 G. The EPR spectrum was fit (red line) with the following parameters: $g_x = g_y = 2.07$, $g_z = 1.993$, $sg_x = 0.04$, $sg_y = 0.08$, $sg_z = 0.022$, D=10cm^{-1}, and E/D=0.032. b) Spin density plot (B3LYP/ TZVP) with important spin density values indicated. Note that the total net spin density of each phenolate ring is about |0.15| (not counting the coordinating O atoms). The spin densities of individual carbons are shown for one of the phenolate rings.
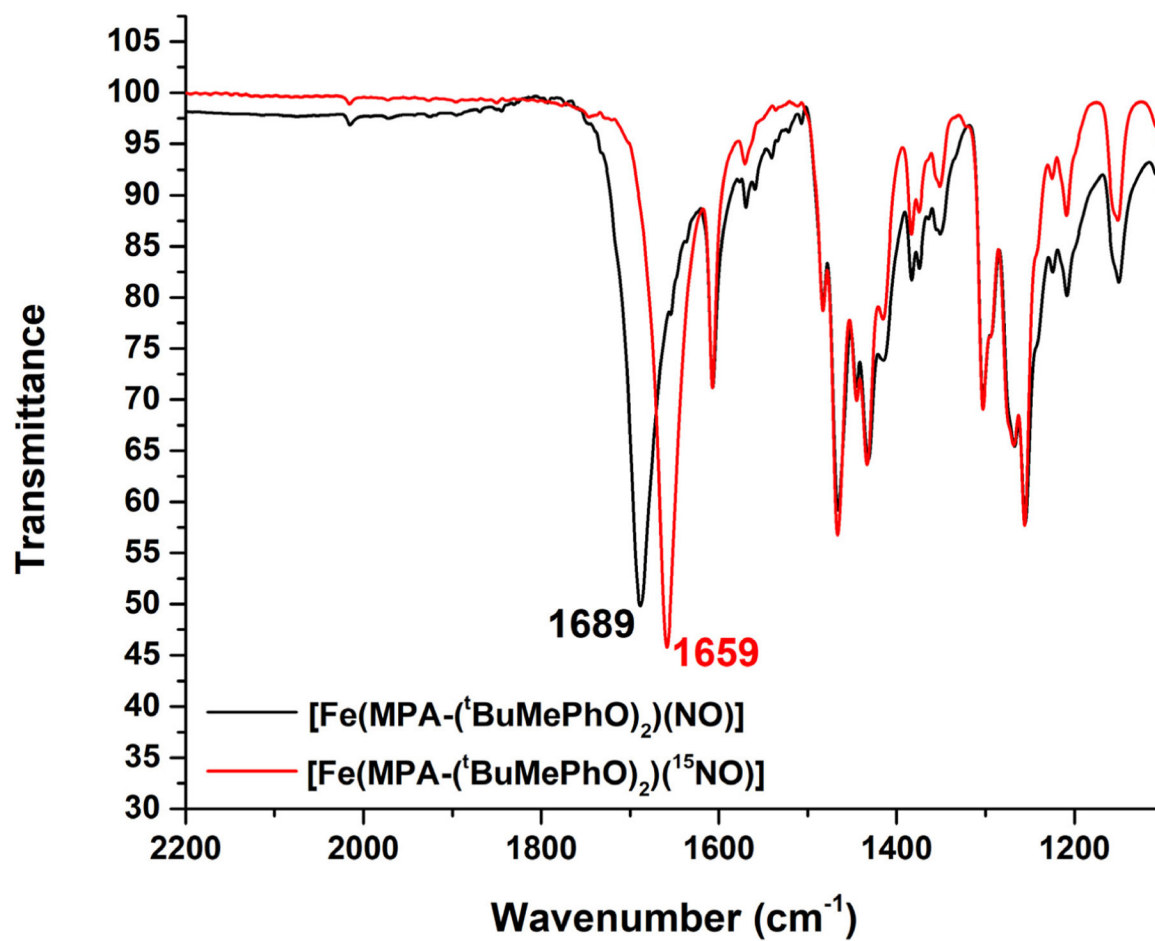
Figure 5.
Solid state IR spectrum of complex **3**, taken in a KBr disk, which shows the N-O stretching frequency at 1689 cm^{-1}. This feature shifts to 1659 cm^{-1} in ^{15}NO-labeled **3**.
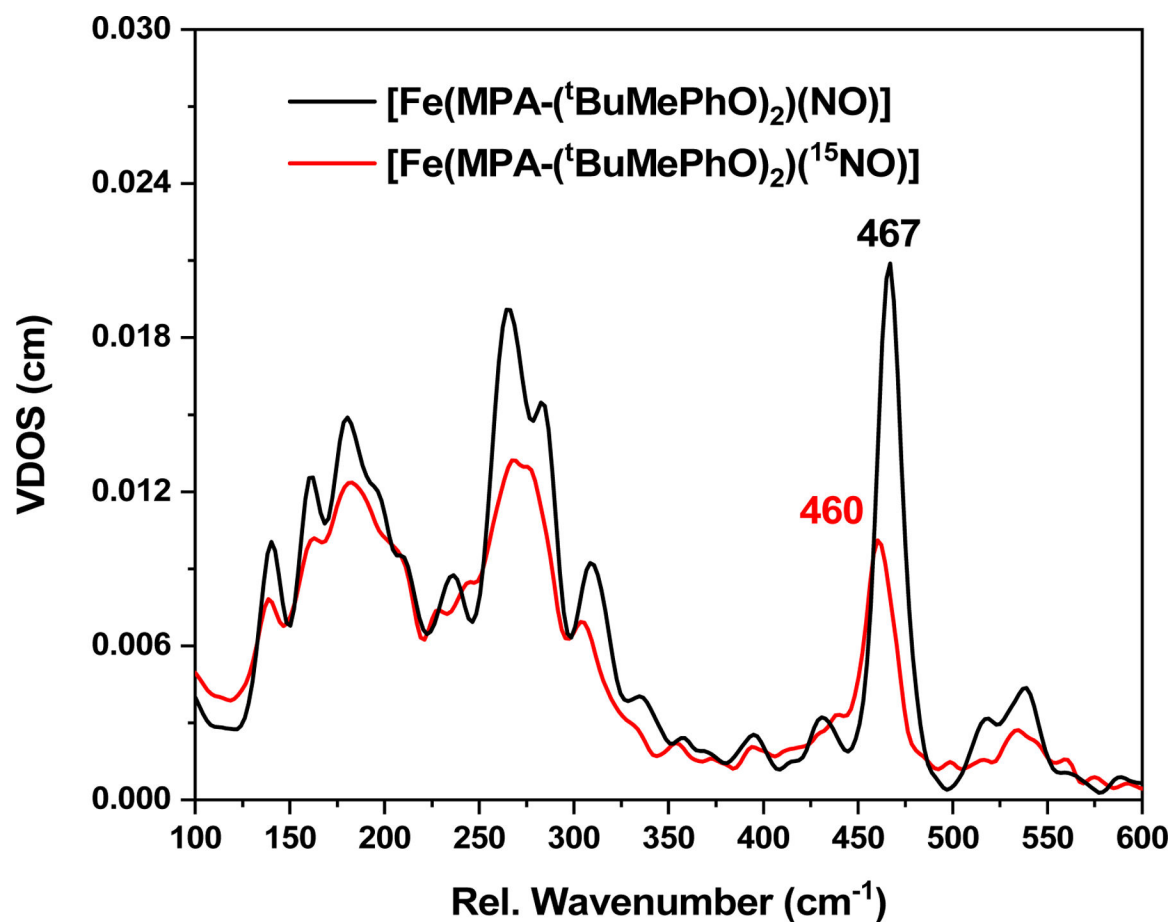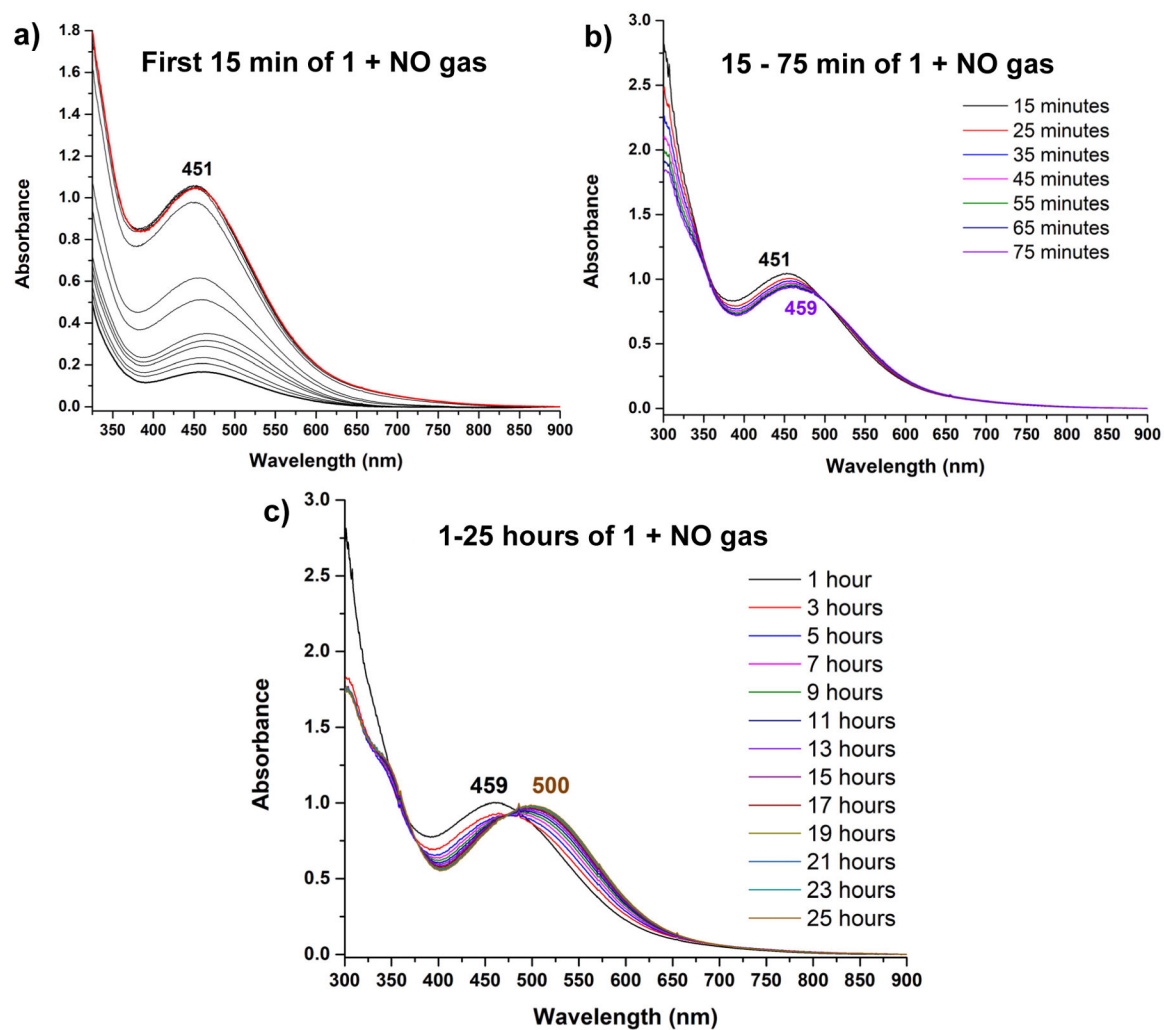
Figure 6.

NRVS data of complex **3** (black) in comparison to the data of the ^{15}NO-labeled analog (red), showing the Fe-NO stretch at 467 cm^{-1}. Note that the difference in intensity of the Fe-NO stretch in the two data sets is due to partial nitrosylation in the reaction with ^{15}NO, due to a lower concentration of the isotopically labeled gas.
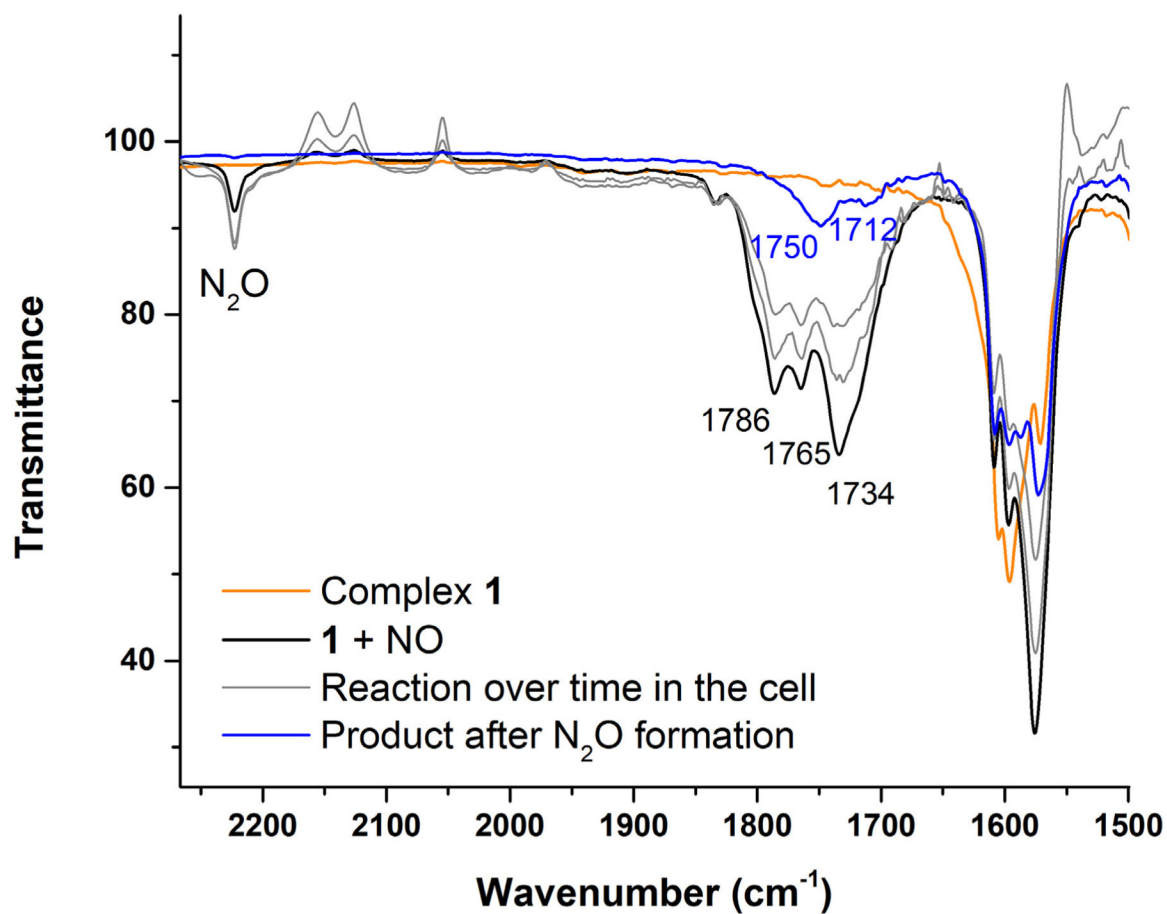
Figure 7.
Fe-NO vs N-O stretching frequency correlation plot, generated from available data in the literature (see also Table S20).[33,62,68] Here, complex **3** extends the correlation to lower frequencies and in this way, helps refine the correlation line (previous fit: black dashed line; revised fit: red line), due to its lowest Fe-NO and N-O vibrational frequencies in the series so far.
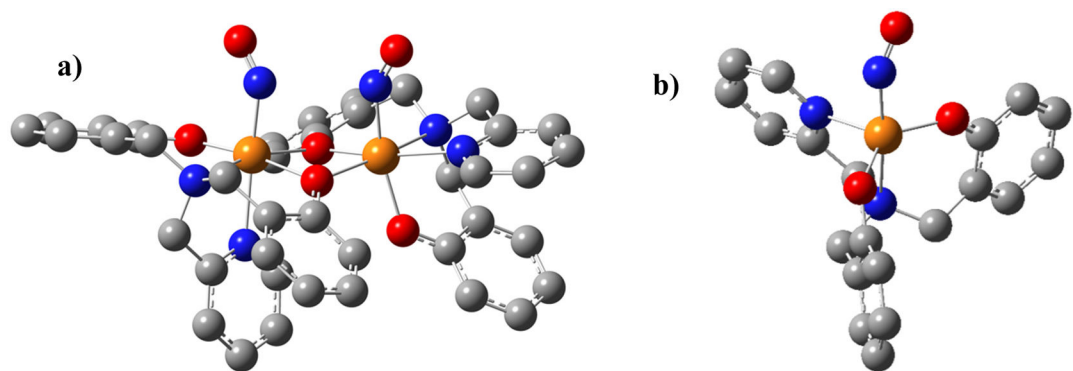
Figure 8.
UV-Vis spectra monitoring the reaction of complex **1** with NO gas in DMF at 0.2 mM concentration at room temperature. The data were collected within 24 hours of the reaction: a) was taken within the first 15 minutes of the reaction (each line: every 1.5 minutes); b) was taken every 10 minutes after that for an hour; c) was taken every 2 hours after that until the reaction is complete at around 25 hours.

Figure 9.
Solution IR spectra of the reaction of complex **1** with NO gas in CH_2Cl_2 at 10 mM concentration, showing the formation of multiple NO complexes right after the addition of NO gas (black line, taken immediately upon adding NO gas) and their disappearance over time (within the first 15 minutes in the IR cell; gray lines), concomitant with formation of N_2O as indicated. The final spectrum in blue was taken after 24 hours (same data as in Figure S12).

Figure 10.
Left: optimized structure (BP86/TZVP) of the putative cis-[{Fe(MPA-(PhO)$_2$)(NO)}$_2$] complex, likely responsible for N$_2$O generation in the reaction of complex **1** with NO gas in DMF at room temperature (see Scheme 3). Right: optimized structure (BP86/TZVP) of the monomeric hs-{FeNO}^{7} complex, [Fe(MPA-(PhO)$_2$)(NO)], which is analogous to complex **3**.

Table 1.

Key geometric parameters and N-O stretching frequencies for complex **3** and select hs-$\{FeNO\}^7$ compounds from the literature with similar coordination geometries.

Compound	Fe-NO [Å]	N-O [Å]	Fe-N-O [deg]	ν(N-O) [cm^{-1}]	δ (mm/s)	EQ (mm/s)	Ref.
[Fe(MPA-(^{t}BuMePhO$_2$)(NO)] (**3**)	1.79	1.15	149	1689 (solid) 1698 (DCM)^b	0.56	0.92	*t.w.*
[Fe(NO)(Me$_3$TACN)(OSi^{Ph2})$_2$O)]	1.76	*n.d.*	144	1680 (THF)	0.52	0.80	[37]
[Fe(BMPA-^{t}Bu$_2$PhO)(NO)(OTf)] (**4**)	1.78	1.10	163	1742 (solid) 1753 (DCM)^8	N/A	N/A	[67]
[Fe(BMPA-Pr)(NO)(Cl)]	1.78	1.15	152	1726 (solid)	N/A	N/A	[62]
[Fe(TMG$_3$tren)(NO)]$^{2+}$	1.75	1.15	168	1741 (solid)	0.48	−1.42	[68]
[Fe(TIMEN^{Mes})(NO)]$^{2+}$	1.76	1.15	179	1803 (solid)	0.31	−0.51	[76]
Deflavo-FDP(NO)$_2$	n.d.	n.d.	n.d.	1749 (aq.)	0.74	1.85	[30]

^{a}Average values for two non-equivalent [FeNO] units

^{b}DCM = dichloromethane

t.w. = this work, *n.d.* = not determined